Photometric properties of Mars soils analogs

A. Pommerol,[1] N. Thomas,[1] B. Jost,[1] P. Beck,[2] C. Okubo,[3] and A. S. McEwen[4]

[1]   We have measured the bidirectional reflectance of analogs of dry, wet, and frozen Martian soils over a wide range of phase angles in the visible spectral range. All samples were produced from two geologic samples: the standard JSC Mars-1 soil simulant and Hawaiian basaltic sand. In a first step, experiments were conducted with the dry samples to investigate the effects of surface texture. Comparisons with results independently obtained by different teams with similar samples showed a satisfying reproducibility of the photometric measurements as well as a noticeable influence of surface textures resulting from different sample preparation procedures. In a second step, water was introduced to produce wet and frozen samples and their photometry investigated. Optical microscope images of the samples provided information about their microtexture. Liquid water, even in relatively low amount, resulted in the disappearance of the backscattering peak and the appearance of a forward-scattering peak whose intensity increases with the amount of water. Specular reflections only appeared when water was present in an amount large enough to allow water to form a film at the surface of the sample. Icy samples showed a wide variability of photometric properties depending on the physical properties of the water ice. We discuss the implications of these measurements in terms of the expected photometric behavior of the Martian surface, from equatorial to circum-polar regions. In particular, we propose some simple photometric criteria to improve the identification of wet and/or icy soils from multiple observations under different geometries.

1.   Introduction

[2] A number of space-borne passive remote-sensing methods rely on the interaction of the solar radiation with planetary surfaces. The relative levels of absorption and reflection of the solar light by the surface materials are the main parameters investigated. The study of the spatial variability of the surface reflectivity (imaging) reveals topographic and some compositional information. The study of the spectral variability of the surface reflectivity (reflectance spectroscopy) provides compositional information. The study of the angular variability of the reflectivity of surfaces, i.e., the dependence of the observed reflectance to the positions of the Sun and the instrument (observer), can also provide additional constraints on the physical state and composition of the surface materials. Because of the complexity of the physics of light scattering in particulate media and the need for multiple images of each surface, this information has probably been the least commonly used in past and current remote-sensing missions.

[3] Models have been designed to link the bidirectional reflectance (r) of a sample to the macroscopic properties of its surface (roughness, density) and to the microscopic properties of its components (optical properties, size, and shape of the grains…) [*Hapke*, 1993; *Mishchenko et al.*, 1996; *Shkuratov et al.*, 1999]. These models can be used to invert photometric measurements of planetary surfaces in order to retrieve the modeled properties. However, because of the large number of free parameters and the intrinsic limitations of the models, careful verification of the accuracy of the inversion process is necessary to acquire confidence in the retrieved parameters. Laboratory measurements on well-characterized samples are crucial for that purpose [e.g., *McGuire and Hapke*, 1995; *Nelson et al.*, 2002; *Shkuratov et al.*, 2002; *Kaasalainen*, 2003; *Piatek et al.*, 2004; *Cord et al.*, 2005; *Gunderson et al.*, 2006; *Shepard and Helfenstein*, 2007; *Pommerol and Schmitt*, 2008; *Hapke et al.*, 2009; *Souchon et al.*, 2011].

[4] In the particular case of Mars, the study of surface photometry is complicated by the presence of a dusty atmosphere [*Ceamanos et al.*, 2013]. Any measurement of the Martian surface from orbit is thus a combination of surface and atmospheric effects. The amount of suspended aerosols in the atmosphere is highly variable, both temporally and spatially

[1]Physikalisches Institut, Universität Bern, Bern, Switzerland.
[2]Institut de Planétologie et d'Astrophysique de Grenoble, UMR 5274, CNRS/Université Grenoble I, Grenoble, France.
[3]U.S. Geological Survey, Astrogeology Research Center Survey, Flagstaff, Arizona, USA.
[4]Lunar and Planetary Laboratory, University of Arizona, Tucson, Arizona, USA.

Corresponding author: A. Pommerol, Physikalisches Institut, Universität Bern, Sidlerstrasse 5, CH-3012 Bern, Switzerland. (antoine.pommerol@space.unibe.ch)

[*Clancy et al.*, 2003; *Vincendon et al.*, 2009]. In addition, fine-grained aerosols scatter the solar light in a strongly anisotropic way and with a strong wavelength dependence [*Clancy et al.*, 2003]. As a result, scattering of light by aerosols in the atmosphere can dominate the bidirectional signal at various wavelengths and in different scattering geometries, with maximal effects at shorter wavelength and around the forward-scattering direction.

[5] However, the presence of aerosols in the atmosphere has also promoted the use of multiangular observations because of their potential to estimate the amount and properties of aerosols [e.g., *Clancy and Lee*, 1991]. The CRISM imaging spectrometer has in particular been designed to acquire systematically multiangular observations, with emission angles varying between $-70°$ and $+70°$ by steps of $10°$, for each high-resolution scene. The inversion of such data sets in terms of both surface and atmosphere properties is challenging but significant progress has already been made, paving the way to a global data set of surface phase functions in the visible and near-infrared spectral ranges [*Ceamanos et al.*, 2013; *Fernando et al.*, 2013; *Vincendon*, 2013]. Because they show different levels of sensitivity to the various compositional and textural parameters, visible-near-infrared spectroscopy and multiangular photometry complement each other and the combination of these techniques is likely to provide better constraints on important surface parameters.

[6] Orbital determinations of the surface reflectance can be locally tested by comparing the retrieved photometric parameters with observations obtained at the surface by landers and rovers [*Fernando et al.*, 2013]. Images obtained by the Mars Pathfinder camera have been used to assemble phase curves of rocks and soils at the landing site [*Johnson et al.*, 1999]. Results show a dominantly backscattering photometric function for all observed materials and forward scattering at high phase angle ($> 140°$) in the case of dark grey rock surfaces. Extensive surveys of the photometric properties of the various soils and rocks observed by the MERs confirm this trend [*Johnson et al.*, 2006a, 2006b]. Reflectance values measured over wide ranges of phase angle ($0–150°$) were fitted by the Hapke model [*Hapke*, 1993] to retrieve a set of Hapke parameters for each of these targets. Undisturbed soils and red rocks (assumed to be coated by red dust) show a predominant broad backscattering behavior whereas grey rock surfaces as well as compressed soils in the wheel tracks show a more forward-scattering behavior. Interpretation of the observed behavior relies on both modeling and comparison with the results of laboratory measurements on well-characterized samples [*McGuire and Hapke*, 1995; *Johnson et al.*, 2013].

[7] Good laboratory measurements of the bidirectional reflectance distribution function (BRDF) of some plausible Mars analogs already exist but are mostly restricted to volatile-free geologic samples. *Nelson et al.* [2002], *Shkuratov et al.* [2002], *Cord et al.* [2003, 2005], *Georgiev and Butler* [2005], *Johnson et al.* [2013], *Shepard and Helfenstein* [2007], *Pommerol and Schmitt* [2008], *Souchon et al.* [2011], and *Johnson et al.* [2013] all measured the photometric properties of geologic samples, including some plausible analogs for the surface of Mars, over various geometries and wavelengths. The comparison of these results shows significant differences of photometric behavior between samples. The interpretation of these differences in terms of

physical parameters appears highly challenging from visible photometry alone, in the absence of complementary information on the sample [e.g., *Shepard and Helfenstein*, 2007; *Gunderson et al.*, 2006].

[8] *Gunderson et al.* [2007] investigated the case of a wet regolith simulant. The objective of this study was to assess the possibility of detecting liquid water in the Martian regolith from orbital visible images. Liquid water was sprayed over a sample of JSC Mars-1 while its reflectance was measured. The reflectance was affected by the addition of water over a wide range of phase angle and at different wavelengths. These results demonstrate the strong effect of liquid water on the sample reflectance, both in terms of overall albedo and shape of the phase function. These measurements have recently proven to be relevant for the interpretation of some of the most intriguing present-day processes on Mars: dark markings appearing each year in spring and disappearing in winter on slopes favorably exposed to sunlight, referred to as Recurring Slope Linae (RSLs) [*McEwen et al.*, 2011; *Chevrier and Rivera-Valentin*, 2012; *Levy*, 2012]. The transient presence of minute amounts of salty liquid water in the Martian regolith, considered as the most plausible hypothesis to explain the RSLs, has also been suggested by in situ measurements at the Phoenix landing site [*Stillman and Grimm*, 2011] and by spectral interpretations [*Cull et al.*, 2010] reinforcing the interest for its detectability by remote-sensing techniques. This work is also relevant to the study of "hypersaline wet patches" in Antarctica's dry valleys, which appear as dark soil patches during spring, in the absence of snow melt. Chemical analyses of these soils [*Levy et al.*, 2012] show that they are enriched in hygroscopic salts as well as in water, pointing to deliquescence of salts as the darkening process.

[9] Extensive bidirectional reflectance measurements of wet terrestrial sediments have been published by *Zhang and Voss* [2006]. Although most of the samples and processes used in this study have little relevance for the case of the Martian surface, the discussion of the observed photometric behaviors in terms of the physical mechanisms that could explain the darkening effect is of general significance. In particular, *Zhang and Voss* [2006] use the measured reflectance data to test two different physical models of wetting-induced darkening [*Twomey et al.*, 1986; *Lekner and Dorf*, 1988] and conclude that neither of these two models can accurately predict the photometric effects of introducing fluids in particulate media. This conclusion reinforces the need for additional theoretical and experimental studies to address this question. One of the six samples studied by [*Zhang and Voss*, 2006], described as "volcanic black beach sand from the big Island, Hawaii (Volcanic)" is potentially relatively similar to the Hawaiian basaltic sand used in this study.

[10] The purpose of this paper is to report extensive measurements of the bidirectional reflectance functions of both volatile-free and volatile-rich analogs of Martian soils. In the case of dry samples, we have acquired new measurements of the photometry of surfaces prepared from JSC Mars-1 soil simulant using different procedures. This material, a Hawaiian palagonitic soil [*Allen et al.*, 1997; *Morris et al.*, 2000; *Hamilton et al.*, 2008], is without doubt the most widely used laboratory analog for the surface of Mars. Its reflectance properties were already measured by a number of investigators allowing us to assess the reproducibility of
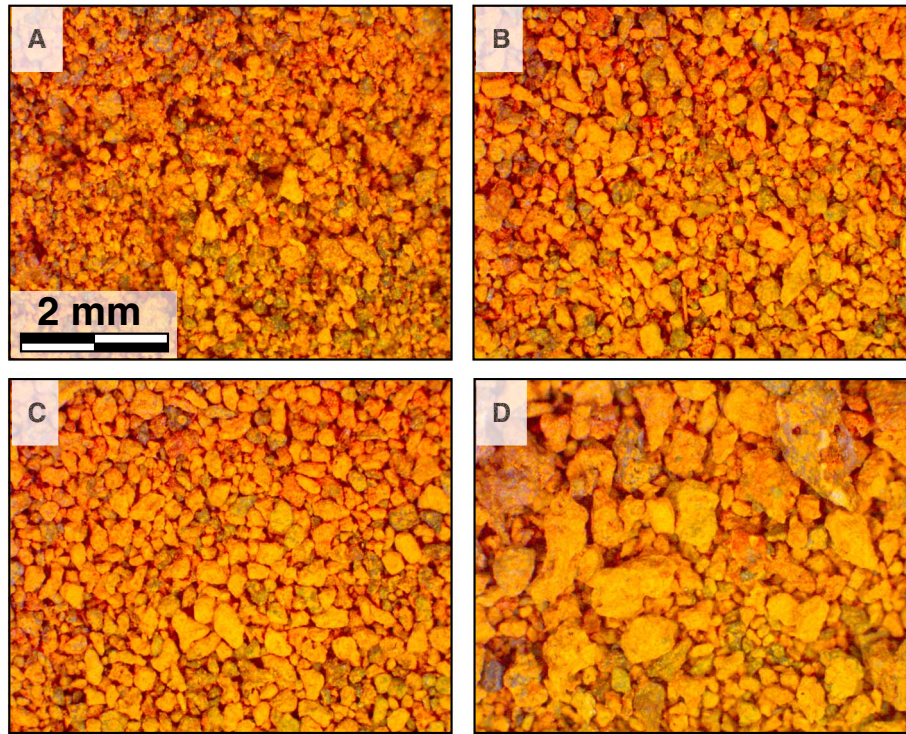
Figure 1. Optical microscope pictures (6×5 millimeters) of the four surfaces prepared with the JSC Mars-1 regolith simulant and for which bidirectional reflectance data were acquired with the PHIRE-2 instrument. Each of the four surfaces was prepared using a different method. (A): the sample holder was initially overfilled and the excess of powder later removed with the edge of a steel spatula to produce a flat surface. (B): powder was sprinkled with a sieve into the holder. (C): a surface composed of sprayed powder was slightly compressed with a smooth and flat surface. (D): the powder was distributed horizontally by shaking the sample holder in a circular manner.

photometric laboratory measurements using different instruments and procedures. To understand the relative variability of observed phase functions, we also prepared surfaces with different textures, starting from the same initial material. In addition to the JSC Mars-1 sample, we also acquired photometric measurements on two particle size fractions of the more pristine Hawaiian basaltic sand, which is probably a better analog than palagonitic soil for the dark regions of Mars.

[11] All these samples were later wetted in order to complement the work of *Gunderson et al.* [2007]. Samples were measured with variable amounts of liquid water over wider ranges of incidence, emission, and azimuth angles. We also report for the first time on the photometry of ice-bearing analogs of Martian soils. A large amount of water ice is known to be present in the Martian surface/subsurface at depths that strongly depend on latitude [e.g., *Feldman et al.*, 2004; *Smith et al.*, 2009; *Byrne et al.*, 2009]. Smaller quantities of seasonal water frost have also been detected over a range of latitudes [i.e., *Vincendon et al.*, 2010; *Pommerol et al.*, 2011a, 2013]. Because of the importance of the detection and quantification of ice for the current inventory of Martian water and for the understanding of present-day climate, we want to investigate the possibility of detecting low amounts of ice at the surface from visible multiangular observations.

[12] For most of the reflectance measurements presented in this paper, we provide series of Hapke coefficients obtained by fitting the Hapke photometric model [*Hapke*, 1993, 2002] to our experimental data. The qualities and limitations of this model and in particular the physical interpretation of the retrieved coefficients have been extensively discussed in the literature [e.g., *Gunderson et al.*, 2006; *Shepard and Helfenstein*, 2007; *Helfenstein and Shepard*, 2011; *Souchon et al.*, 2011; *Hapke*, 2012; *Shkuratov et al.*, 2012; *Hapke*, 2013]. It is not an objective of this study to further test the photometric model. Hapke parameters are essentially provided here to allow reproducing our data and facilitate the comparisons with other laboratory or planetary data sets, interpolating and/or extrapolating them to nonmeasured geometries and integrating the bidirectional reflectance values to calculate integrated photometric properties such as physical albedos or integral phase functions. Because the physical meaning of these parameters is still unclear, their values will not be extensively discussed in this article. We provide, however, ranges of uncertainties for the determination of all parameters and the classical "hockey stick" plot (see [*Hapke* 2012]), so that these parameters can be analyzed in more details and compared to other studies by interested readers.

[13] The PHIRE-2 (PHysikalisches Institut Radiometric Experiment - 2) instrument, which has been used to acquire all photometric measurements reported in this paper, as well as the calibration procedure and estimates of uncertainties are presented in the Methods Section together with the numerical methods used to fit the data and retrieve the Hapke parameters. The Results Section then presents the photometric measurements together with microscopic images of the samples that are invaluable for the interpretation of the observed
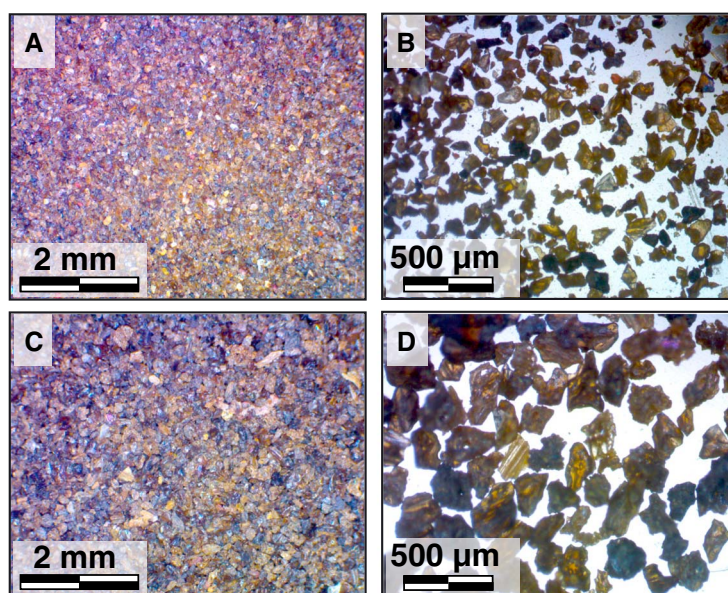
Figure 2. Optical microscope pictures (6×5 millimeters) of the two size fractions of Hawaiian basaltic sand used in this work: fine (sieved $< 109\,\mu m$, pictures A and B) and coarse ($109\,\mu m$–$1\,mm$, pictures C and D). Pictures A (fine: $< 109\,\mu m$) and C (coarse: $109\,\mu m$–$1\,mm$) on the left show the surfaces of the samples from which the photometric measurements were acquired while pictures B (fine) and D (coarse) on the right show the individual grains observed in transmission mode.

photometric behavior. The implications of the results for analyses of the state and composition of the Martian surface by optical remote sensing are the subject of the Discussion Section. The main results are finally summarized in the Conclusion Section where potential perspectives for future studies are also discussed.

2. Samples and Methods

2.1. Samples

2.1.1. Nature of Geologic Samples

[14] Two types of geologic samples were used in this study: the JSC Mars-1 regolith simulant [*Allen et al.*, 1997; *Morris et al.*, 2000; *Hamilton et al.*, 2008] and a Hawaiian basaltic sand sample.

[15] JSC Mars-1: The JSC Mars-1 sample is a common analog for Mars surface distributed by the NASA Johnson Space Center. It consists of the $< 1\,mm$ size fraction of a soil collected on the Pu'u Nene Cinder cone in Hawaii [*Allen et al.*, 1997] and is described as a palagonitic tephra [*Morris et al.*, 2000; *Hamilton et al.*, 2008]. This natural terrestrial material closely matches the visible and near-infrared reflectance of the bright regions of Mars. Close-up views of four surfaces prepared using this material are shown in Figure 1. The chemical composition of JSC Mars-1 shares properties with the one measured at the Viking-1 landing site. In addition to its intrinsic qualities as a Mars soil analog, a strong advantage of this material is that large quantities were made available to the community, which led to the acquisition of comparable or complementary measurements in different facilities. It is therefore a good sample to check for the reproducibility and consistency of measurements.

[16] Hawaii Basalt: Whereas JSC Mars-1 is a good photometric and spectral analog for intermediate to high albedo red regions of Mars, many other regions of Mars show a much lower albedo and a dark grey color. This is in particular the case of terrains where RSLs are observed and the North polar erg where Phoenix landed. Infrared spectral analyses of Martian dark terrains [*Bandfield*, 2002; *Poulet et al.*, 2007] indicate a basaltic composition. As plausible analog for the low-albedo regions, we have thus acquired photometric measurements on a more pristine basaltic sample. The sample of basalt used in this study has been collected from active dunes in the Ka'u Desert region along the southwest flank of Kīlauea volcano, Hawai'i by C. Okubo. It is a mixture of tephra and basalt that has been eroded and transported by fluvial and eolian processes. The sand was dry sieved to separate two particle size fractions: less than $109\,\mu m$ ("fine fraction") and between $109\,\mu m$ and $1\,mm$ ("coarse fraction"). Figure 2 shows optical microscope pictures of grains from the two particle size fractions (Figures 2B and 2D) as well as smooth surfaces prepared with these particles (Figures 2A and 2C) by slightly compacting sprayed powder with a flat Teflon surface. Despite the fact that the sample was sieved dry, visual inspection under the microscope did not reveal the presence of fine particles clinging to the surfaces of larger ones.

2.1.2. Preparation of Dry Samples

[17] In order to measure their photometric properties, a few grams to tens of grams of the sample powder were placed in round sample holders. We have developed different procedures that can result in significant differences in the surface texture of the resulting samples. Optical microscope pictures (Figure 1) show the surfaces of four samples prepared from the same JSC Mars-1 powder using four different preparation procedures. Sample (A) was produced by overfilling the sample holder, then removing the excess of material with the edge of a steel spatula; sample (B) by sprinkling powder directly into the sample holder with a sieve; sample (C) by flattening the sprayed powder, slightly compressing it with a smooth Teflon surface. Sample (D) was produced by

depositing a large amount of material in the center of the sample holder, then spraying it horizontally by shaking the sample holder in a circular manner. This last preparation procedure results in a strong radial segregation of the grains of different sizes. As is clearly visible in Figure 1D, the center of the sample holder from which the photometric measurements were acquired is occupied by the largest grains. In a similar manner, two types of surfaces were prepared with each particle size fraction of the basaltic sand. We prepared "sprinkled" surfaces using the same procedure as the one described to produce surface type B with the JSC Mars-1 and "smooth" surfaces similar to surface type C for JSC Mars-1.

2.1.3. Preparation of Wet Samples

[18] We used the same technique as *Gunderson et al.* [2007] to wet the samples. Water was added to the dry sample by spraying an aerosol of very fine droplets over its surface. Before and after each addition of water, the total mass of the sample was accurately measured to determine its bulk water content. Most of the time, this bulk value is of little importance for the photometric measurements presented below. Because of the slow diffusion of liquid water from top to bottom in the samples and constant drying at the surface, vertical gradients in the sample are likely to result in different values of water content at the surface (which influences the photometry) and at depth. Optical microscope pictures, taken at each step shortly before and after the photometric measurements, provide more relevant, albeit purely qualitative, information on the surface of the sample and the state of water.

[19] We have conducted a single long-term drying experiment in which a sample of JSC Mars-1 was initially saturated in liquid water and then left to dry while photometric measurements were regularly acquired. The sample was also regularly moved from the photo-goniometer to the optical microscope to acquire pictures of its surface. This experiment was conducted until the sample completely dried out, after several weeks, in order to compare the initial and final dry states.

[20] In order to test the effect of brine crystallization on the photometric properties of the dried samples, we have also wetted a basalt sample with water in which sodium chloride had previously been dissolved until saturation. The sample was then left to dry until all liquid water had completely evaporated resulting in the formation of a crust of salt at the surface. Microscope pictures and bidirectional reflectance data of this surface were then acquired.

[21] For all the wetting and drying experiments described here, the initial dry material was prepared by spraying powder into the sample holder with a sieve, which corresponds to surface B for the JSC Mars-1 material (Figure 1) and to the surfaces referred to as "sprinkled" for the coarse and fine basalt samples.

2.1.4. Preparation of Icy Samples

[22] Several procedures were tested to produce different types of "icy" samples. First, wet samples produced according to the procedure detailed in section 2.2.3 were placed in a freezer at a temperature of 243 K. This systematically resulted in the formation of a matrix of ice around the grains in the bulk of the sample whereas the upper parts of the grains at the surface of the sample remained completely free of ice. Pictures of one of the samples prepared in such a way ("frozen A"), as well as other icy samples described in the following paragraphs, are presented in the Result Section, together with

the corresponding photometric measurements. The thickness of the desiccated upper layer was variable, depending on the initial amount of water and the nature of the geologic sample.

[23] In order to cover completely the surface of the samples with ice, liquid water was sprayed onto the icy samples. The immediate freezing of the water at the contact with the cold grains results in the formation of a continuous, conformal, and transparent thin film of water ice over the surface. By spraying the liquid water with different durations, one can easily vary the thickness of the ice film. Sample "frozen B" was prepared in order to obtain a very thin ice film on top of the grains. Sample "frozen C" was prepared in order to obtain a much thicker film of water ice that fills the gaps between grains and thus hides the topography of the underlying surface.

[24] Finally, in order to test the influence of frost deposition on the grains, icy samples previously stored at 243 K in the freezer were exposed for a few minutes to the ambient laboratory atmosphere while their surface was continuously observed under the microscope. Large amounts of frost condense over the grains by cold trapping of the ambient water vapor. The sample was then carefully transported to the photo-goniometer where photometric measurements were conducted. In the dry atmosphere of the freezer and at a constant temperature of 253 K, the surface frost was observed to steadily sublime, allowing us to study the temporal evolution of photometry induced by the disappearance of frost. Because the sublimation of ice was taking place rapidly, we limited the number of different geometries measured to increase the temporal resolution. In this configuration, the entire sequence of measurements could be repeated every 3 min.

2.2. Reflectance Measurements

2.2.1. Instrument

[25] All the new measurements reported here have been acquired with the PHIRE-2 instrument at the University of Bern, a photo-goniometer installed in a large freezer and designed to operate within $+/-$ 35 K of freezing point. A complete description of this instrument is provided by *Pommerol et al.* [2011b]. Only the information that is fully relevant for this work is provided in the following paragraphs.

[26] The PHIRE-2 instrument permits the measurement of the photometric properties of cm-sized samples in separated broad wavelength bands in the visible and near-infrared spectral range (400–1100 nm). At the time when these measurements were obtained, the instrument was equipped with six band-pass filters with central wavelengths at 450, 550, 650, 750, 905, and 1064 nm. The Full Width Half Maximum (FWHM) bandwidth was 70 nm for the first four filters and 10 nm for the last two (905 and 1064 nm).

[27] The incident light onto the sample is a collimated beam with a diameter of 20 mm. The length of the illuminated area on the sample varies proportionally to the cosine of the incidence angle. The size of the sample is thus limiting the maximum achievable incidence angle. The sample holders used for most of the measurements reported here were plastic Petri dishes, 10 mm thick and 100 mm diameter. Using such sample holders, the maximum achievable incidence angle is 70°. By design of the instrument, reflectance measurements are also restricted to phase angles larger than 5°. The field of view of the detector is set so that it

encompasses the entire illuminated area of the sample. The angular field of view of the detector corresponding to this illuminated area, which defines the angular resolution of the system, depends on the incidence, emission, and azimuth angles. For the sets of geometries used in this paper (see section 2.2.4), the full solid angle varies between 0.5° and 6° and thus only rarely and very slightly exceeds the finest angular sampling used during measurements (5°).

2.2.2. Calibration

[28] We calibrate all measurements by normalizing the raw voltage signals to a single reflectance measurement of the reference surface Spectralon (Labsphere) obtained at a vertical incidence: $i = 0°$ and emission: $e = 55°$. This calibration procedure was first described by *Gunderson et al.* [2007] and has already proven its robustness by comparison with similar measurements performed on other facilities [*Pommerol et al.*, 2011b]. Using this method, the reflectance data are calibrated in units of bidirectional reflectance (r) and can then be converted in units of radiance factor (RADF), bidirectional reflectance distribution function (BRDF) or reflectance factor (REEF) using equations 10.1, 10.3, and 10.5 in *Hapke* [1993]. All measured and calculated values of reflectance presented in this article are in units of "reflectance factor" (REFF), the ratio between the actual reflectance of the sample measured in a particular geometry and the one of a hypothetical perfect Lambertian diffuser measured in the same geometry. In this unit, a prefect Lambertian diffuser would have a reflectance factor of one in any geometry. The reflectance factor (REFF) is related to the bidirectional reflectance (r) by the relation: $REFF = r * \pi / \cos i$, to the bidirectional reflectance distribution function (BRDF) by the relation: $REFF = BRDF * \pi$, and to the radiance factor (RADF) by the relation: $REFF = RADF / \cos i$.

[29] The surface of the samples, despite careful preparation procedures, can never be made perfectly flat and horizontal. In practice, sample preparation often results in surface tilts of a few tenths of a degree and up to 1° or 2° in some extreme cases. Because the calibration procedure involves divisions of raw values by the cosines of the incidence and emission angles, small errors in the determination of the angles (which are defined relative to the local normal to the surface) will have a nonnegligible effect at high incidence and emission angles. We have thus developed a method to correct at first order the effects of sample tilt. We assume that the surface of the sample is flat but tilted relative to the horizontal plane. The orientation of the surface can be described by two tilt angles, one in the principal plane (i.e., vertical plane containing the incidence direction, azimuth = 0° and 180°) and one in the perpendicular plane (azimuth = 90° and 270°), which result from the projection of the total surface tilt vector on these two planes. These two angles can be accurately determined from measurements performed at vertical incidence for multiple emission (30 to 80°) and azimuth (0, 90, and 180°) angles. For a vertical incidence, the values of reflectance factor should display a radial geometry around the vertical and any observed discrepancy to this symmetry is assumed to originate from the sample tilt. The tilt in the principal plane is determined from the comparison of the reflectance values measured for azimuth = 0° and 180°, respectively, by searching the optimal angle to correct the dissymmetry. The same procedure is then repeated in the perpendicular plane, by comparing the values of reflectance obtained for azimuth = 90° with values obtained for azimuth = 0°. Once both the principal plane and the perpendicular plane tilts have been determined, the entire coordinate system can be rotated by the determined rotation vector and the reflectance factor values recalculated using the corrected values of incidence and emission angles.

2.2.3. Measurements Uncertainties

[30] The stability, repeatability, and signal to noise ratio of the instrument were carefully characterized and allowed us to derive relative uncertainties of $\pm 2\%$ on the measured reflectance values, maximal at high emission angle due to slight mechanical imperfections and optical misalignments (see [*Jost et al.*, 2013], for more details). This high stability results from a series of technical improvements, which significantly improved the performance of the instrument since the first measurements were acquired [*Pommerol et al.*, 2011b]. In addition to instrumental characterizations, we can assess the accuracy of the measurements from the data themselves, by comparing the reflectance of couples of points corresponding to alternate positions of the light source and the detector. Because the values of reflectance in these two positions should by definition be identical: $REFF(i,e,g) = REFF(e,i,g)$ ("Reciprocity principle", equation 10.9b in [*Hapke* 1993]), these comparisons offer a robust way to evaluate the errors resulting from a number of different sources, including instrumental errors and the effects of the spatial inhomogeneity of the sample. We typically observe standard deviations between 1 and 2% (depending on the sample texture), in good agreement with independent estimates of instrumental accuracy. A 1-σ relative error of 2% is thus considered for all data presented in this paper.

2.2.4. Data Sets and Data Display

[31] We have measured the reflectance factors of all samples at incidence angles of 0° and 30°. Depending on the sample, additional measurements were obtained at various incidence angles between 10° and 70°. For each incidence angle, reflectance was measured for emission angles varying between 0° and 80° in steps of 5° and for azimuth angles varying between 0° and 165° in steps of 15°. This represents a total of 192 data points in one half of the upper hemisphere for each incidence angle. This set of 192 points in spherical coordinates is then linearly interpolated to Cartesian coordinates on a regular 180×90 pixels matrix using Delaunay triangulation. For reasons of symmetry, the other half-hemisphere can be obtained by mirroring the measured half-hemisphere relative to the principal plane. The entire sequence of measurements was then repeated for each of the different band-pass filters.

[32] Most of the reflectance data in the Results Section are presented in the form of color-coded polar plots. Each of these plots displays the values of reflectance factor as a function of emission and azimuth angles, for a fixed incidence angle, following a rainbow color scale shown on the left. We systematically use here a double colorbar to easily visualize both the absolute level of reflectance of the sample (left colorbar, fixed scale from 0 to 1) and the relative variations of reflectance inside a single plot (right colorbar, stretched between the minimum and maximum values of reflectance displayed in the polar plot). Faint dashed circles are iso-lines of emission angle, from 0° at the center, to 90° on the external circle. The direction of incident light is always on the right side of the diagrams, and apparent as a white "hole"

corresponding to the area where measurements are not possible with the setup used (i.e., phase angles lower than 5°). The principal plane is the median horizontal line which separates the plot in two vertically mirrored half-disks.

[33] The measurement of each of the reflectance factor data sets represented in the polar plots lasts about 20 min. This duration has to be multiplied by the number of desired incidence angles and by the number of desired wavelengths. Thus, the measurement of a typical complete data set (three different incidence angles, six different wavelengths) lasts about 6 h. While this is acceptable for stable samples, it can become problematic for samples that evolve with time such as wet and frozen soils. In cases of fast evolving samples, we have either restricted our measurements to the principal plane (azimuth = 0°) or have only acquired measurements at one given incidence angle (i = 30°) and with a single filter (λ = 650 nm). In the former case, results are represented as classical 2D plots, where reflectance factor is plotted as a function of emission angle for a fixed incidence angle. This way of representing data was also adopted for the comparison of measurements of JSC Mars-1 samples on different instruments, as data out of the principal plane were not available in all data sets.

2.3. Data Fitting

[34] The Hapke model [*Hapke*, 1993, 2002] is certainly the most used photometric model in the planetary remote-sensing community. It relates the optical properties of individual particles (single scattering albedo and single scattering phase function) to the bidirectional reflectance of a surface composed of these particles by modeling the scattering of light between the particles and the influence of macroscopic surface parameters such as surface roughness or density.

[35] Various versions of this model have been published, which differ by the level of accuracy of analytical approximations to complex physical processes and the use of empirical functions to represent photometric behaviors observed experimentally. The simplest version [*Hapke*, 1993] is known as Isotropic Multiple Scattering Approximation (IMSA) in which only the first scattering is considered anisotropic whereas multiple scattering of light between grains is treated as isotropic. The 2002 version of the model [*Hapke*, 2002] allows calculating anisotropic multiple scattering, an improvement thought to be necessary to analyze the reflectance of bright surfaces composed of anisotropic scatterers such as icy surfaces. Another difference between various versions of the model is the analytic approximation of the Ambartsumian–Chandrasekhar *H*-functions, which impacts both the accuracy of the model and the calculation time. We have extensively tested the different formulations of the Hapke model when fitting the model to our experimental data. We concluded that the assumption of isotropic multiple scattering is perfectly appropriate in the case of our geologic samples as no difference could be observed in modeled reflectance curves when considering or not the multiple scattering as anisotropic. This result is expected for samples with a low single scattering albedo. Similarly, we observed that the definition of the H function had a negligible impact on the results. Because the increase in calculation time induced by the choice of the most accurate approximation ([*Hapke*, 2002]) was not significant, we decided to always use this version for data fitting.

[36] The scattering of light by individual particles is parameterized by the single scattering albedo, ω, and an empirical single particle scattering function, which describes the phase dependence of the scattering by isolated particles. Henyey-Greenstein (HG) functions [*Henyey and Greenstein*, 1941] are traditionally used for that purpose. These functions can use one, two, or three independent parameters to describe the forward to backward scattering ratio and the width of the scattering lobes. Note that different versions of the HG functions with confusing naming of the parameters can be found in the literature. Here, we follow the definitions of *Hapke* [2012] for the two-term HG function:

$$p(g) = (1+c)/2*(1-b^2)/(1-2*b*\cos g + b^2)^{3/2}$$
$$+ (1-c)/2*(1-b^2)/(1+2*b*\cos g + b^2)^{3/2} \quad (1)$$

where g is the phase angle, b is the shape parameter that describes the width of the scattering lobes, and c is the backscattering parameter. The first term in equation 1 describes the backscattering lobe and the second term the forward-scattering lobe. The particle is mostly backscattering when $c > 0$ and mostly forward scattering when $c < 0$. For data fitted using a two-term HG function, it seems that the b and c parameters are strongly correlated. The empirical relationship between these two parameters is described by *Hapke* [2012] as the "Hockey-stick relationship" and possible physical causes are proposed.

[37] After experimenting with different versions of the Henyey-Greenstein functions, we have decided to only provide one set of parameters using a two-term HG function. The use of a three-term HG sometimes resulted in better fits in terms of the final difference between data and model but at the price of having most parameters completely unconstrained. The use of a one-term HG function resulted in a significantly degraded quality of the fits.

[38] Note also that the Hapke model is not relevant for some of the samples presented in this paper, as the inclusion of a fluid (water) or a solid matrix (ice) between particles violates one of the fundamental hypotheses of the model, which is that the scatterers behave as independent individual particles. In some cases, it is still possible to fit the data accurately enough (i.e., the model correctly reproduces the general trends observed on measured data) and the values of Hapke parameters are thus reported (wet samples with low to intermediate amounts of water). In other cases (presence of a specular peak in particular), the data simply cannot be fitted by the Hapke model and no parameters are reported.

[39] One of the Hapke parameters defining the amplitude of the opposition effect, the parameter B_s, is theoretically limited to a maximum value of 1. However, some authors decided to leave it free, as it provides better fits to data (for example [*Gunderson et al.*, 2007]) whereas other authors did not notice significant improvement when leaving it free to reach values higher than 1 (for examples [*Johnson et al.*, 2013]) and argue that keeping it limited to 1 results in better constrained sets of Hapke parameters. This was also the case for most of our samples, except the powders covered by fine water frost for which the curves are only fitted correctly by the Hapke model when leaving B_s free to reach values as high as 5. We have thus decided to limit B_s to 1 for all dry and wet samples and left it free to reach higher values for samples covered with H_2O frost.
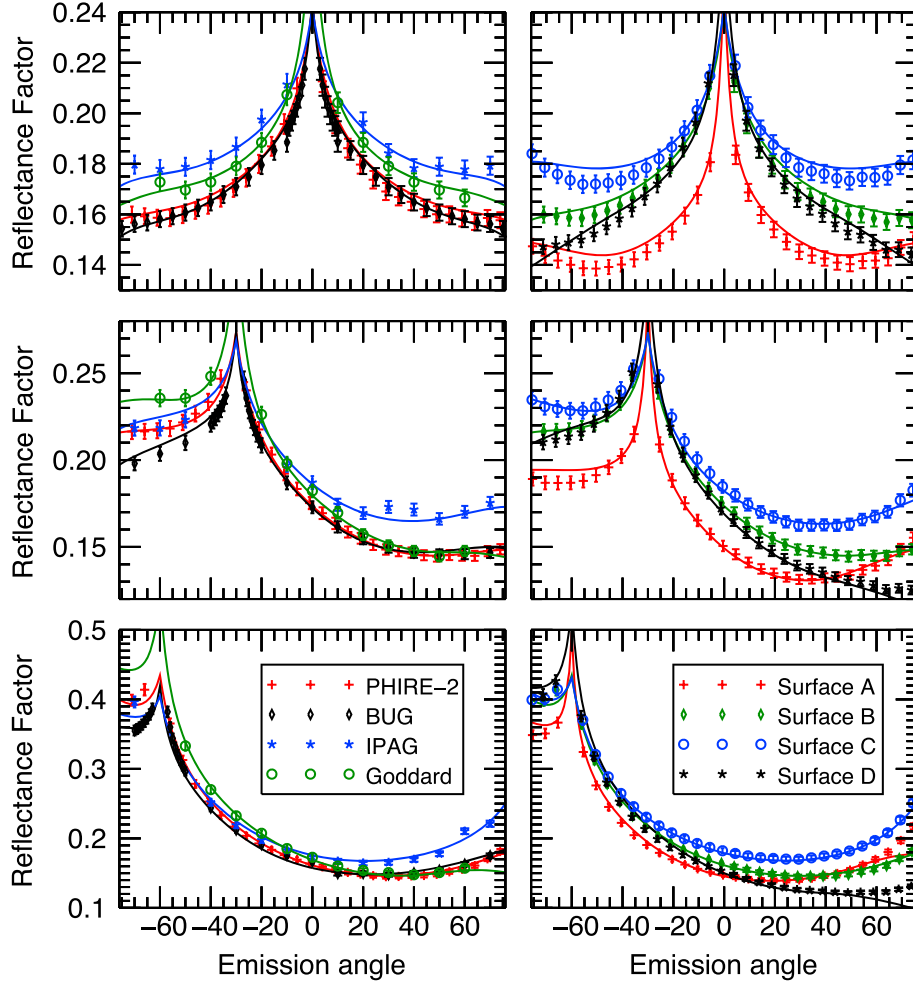
Figure 3. Reflectance factors (symbols) in the principal plane measured for seven different samples prepared with the JSC Mars-1 regolith simulant, with four different instruments. Left column: comparison of reflectance data measured with the PHIRE-2 (Bern, this work), BUG (Bloomsburg, *Shepard and Helfenstein*, [2007]; *Johnson et al*. [2013]), Goddard (Washington, *Georgiev and Butler* [2005]), and IPAG (Grenoble, *Brissaud et al.* [2004], this work). All measurements were acquired in the wavelength range: 650 – 680 nm. Right column: comparison of reflectance data of samples prepared in four different ways, all measured with the PHIRE-2 instrument. Top row: incidence: i = 0°, middle row: i = 30°, bottom row: i = 60°. The solid curves are calculated from the Hapke coefficients (provided in Tables 1 and 2) obtained by fitting the Hapke photometric model to the measured data.

[40] Fitting the Hapke photometric model to large experimental data sets becomes computationally challenging as the angular sampling and ranges increase in the three dimensions of the spherical coordinates system. While a variety of fitting techniques has already been employed in previous studies [*Helfenstein and Shepard*, 2011; *Cord et al.*, 2003; *Gunderson et al.*, 2006; *Johnson et al.*, 2006a, 2006b], we have decided, after experimenting with various algorithms, to use another fitting method combining the Particle Swarm Optimization (PSO) technique [*Kennedy and Eberhard*, 2001] with the Levenberg-Marquart (LM) [*Marquardt*, 1963; *Moré*, 1978, *Markwardt*, 2009] algorithm. These two methods have indeed complementary advantages that make their joint use for photometric data fitting particularly efficient. The PSO technique has the advantage of being able to find a solution for the problem without any initial guess on the parameters while the LM algorithm can quickly refine the approximate

solution found by the PSO to provide the final set of parameters. The optimal solution for a data set containing two thousands reflectance values can typically be found in a few seconds with this technique. The goodness of fit is classically expressed by the total and reduced chi-square, χ^2 and χ^2_{red}, respectively:

$$\chi_{red}{}^2 = \frac{1}{\nu}\chi^2 = \frac{1}{\nu}\sum_N \frac{(Measure - Model)^2}{\sigma^2} \qquad (2)$$

[41] Where σ is the standard deviation of the measurements and ν is the degree of freedom of the problem, equal to the difference between the number of points measured and the number of parameters fitted. A value of $\chi^2_{red} = 1$ indicates the best possible fit (i.e., the difference between the data and the best fit is consistent with the measurement error). Values of χ^2_{red} larger than 1 indicate discrepancies between

Table 1. Hapke Parameters Calculated From PHIRE-2 Reflectance Measurements of the Four Surfaces Prepared With the JSC Mars-1 Sample, Performed at the Wavelength: 650 nm (Figures 3 and 4)[a]

	ω	h_s	B_s	$\bar{\theta}$ (°)	b	c	χ^2_{red}
JSC Mars-1, Surface A	0.526	0.083	1.0	13.3	0.187	0.273	**1.4**
	(0.52, 0.53)	(0.07, 0.10)	(>0.95)	(13, 14)	(0.18, 0.19)	(0.23, 0.31)	
JSC Mars-1, Surface B	0.549	0.056	0.921	16.3	0.179	0.806	**2.0**
	(0.54, 0.55)	(0.04, 0.08)	(>0.83)	(16, 17)	(0.17, 0.19)	(0.76, 0.86)	
JSC Mars-1, Surface C	0.603	0.043	0.936	14.1	0.189	0.452	**1.9**
	(0.60, 0.61)	(0.04, 0.06)	(>0.80)	(14, 15)	(0.18, 0.19)	(0.41, 0.49)	
JSC Mars-1, Surface D	0.499	0.071	0.962	17.4	0.167	1.282	**2.6**
	(0.49, 0.50)	(0.05, 0.10)	(>0.89)	(17, 18)	(0.15, 0.18)	(1.21, 1.38)	

[a]The parameters were retrieved by fitting the isotropic multiple scattering version of the Hapke model to data using a two-terms Henyey-Greenstein function. ω is the single scattering albedo. h_s and B_s the width and intensity of the shadow hiding opposition effect (SHOE), respectively. $\bar{\theta}$ is the mean slope angle (in degrees) that defines the macroscopic roughness of the sample. b and c are the two Henyey Greenstein parameters that define the shape of the single particle scattering function. See *Hapke* [1993] for additional descriptions of these parameters. Ranges of uncertainty on the determination of each parameter are provided below the best fit values, with a resolution of 0.01 for all dimensionless parameters and a resolution of 1° for $\bar{\theta}$. The methods used to determine the best fit values and the ranges of uncertainty are described in section 2.3.

the model and the data whereas values of χ^2_{red} lower than 1 indicate an overfitting of the data by the model.

[42] It is well known that many parameters of the Hapke model are correlated. As a result, the measure of the goodness of the fit cannot be simply used to retrieve ranges of uncertainties for Hapke parameters. Various techniques have been used to estimate these ranges of uncertainties, sometimes leading to contrasted results [*Gunderson et al.*, 2006; *Johnson et al.*, 2006a, 2006b; *Shepard and Helfenstein*, 2007]. We follow here the method proposed by *Gunderson et al.* [2006], where all parameters are successively shifted from their optimal values and other parameters left free to compensate the perturbation to provide a new set of Hapke parameters and a corresponding new χ^2. Then, for each parameter, a range of uncertainty is defined as the range where solutions could be found with a χ^2 smaller than the χ^2 for the optimal solution plus a confidence threshold: $\chi^2 < \chi^2_{best} + \Delta\chi^2$. The 1-$\sigma$ confidence threshold for the Hapke model with six free parameters is calculated by [*Gunderson et al.*, 2007]: $\Delta\chi^2 = 7.034$.

3. Results

3.1. Volatile-Free Analogs

[43] The JSC Mars-1 regolith simulant is the most widely used analog for Martian soils. Prior to this study, photometric and spectral properties of this material were reported by different teams using different instruments. The direct comparison of four of these data sets (Figure 3) provides invaluable insights into the reproducibility of photometric measurements. The three left plots in Figure 3 show measurements obtained at Bloomsburg University with the Bloomsburg University Goniometer (BUG) instrument [*Shepard and Helfenstein*, 2007; *Johnson et al.*, 2013] and archived on the PDS (http://pds-geosciences.wustl.edu/missions/labdata/marsbug.htm), at NASA Goddard Center [*Georgiev and Butler*, 2005], at Institut de Planétologie et d'Astrophysique de Grenoble (IPAG) with the spectro-radio-goniometer [*Brissaud et al.*, 2004], and at Bern University with the PHIRE-2 instrument [*Pommerol et al.*, 2011b]. In addition, the JSC Mars-1 sample measured with the PHIRE-2 instrument was also measured in the exact same conditions with the PHIRE instrument [*Gunderson et al.*, 2006] and both measurements gave nearly indistinguishable results, as previously reported by *Pommerol et al.* [2011b].

Note that all measurements compared here were performed on the unprocessed <1 mm diameter fraction, as distributed by NASA JSC, whereas measurements of different size fractions have also been published (<45 microns in [*Johnson et al.*, 2013]).

[44] The wavelength ranges at which these measurements were obtained are slightly different: 650 nm (FWHM: 70 nm) for measurements in Bern, 680 nm (FWHM: 10 nm for measurements in Grenoble, 650 nm (FWHM: 12 nm) for measurements in Goddard, and 670 nm (FWHM: 50 nm for measurements in Bloomsburg). These differences of wavelength ranges can result in minor vertical shifts of the curves but are unlikely to affect their shapes.

[45] The consistency between the photometric data obtained by four different teams using five different instruments and four different procedures for sample preparation is satisfactory, with maximum discrepancies of the order of 10–15% and very similar general trends. All measured data are also satisfactorily fitted by the Hapke photometric model [*Hapke*, 1993;2002] and the resulting Hapke coefficients are presented in Table 1. As already noted in previous studies, the JSC Mars-1 soil simulant scatters light anisotropically with a maximum of reflectance at low phase angle (backscattering peak). There is more than a factor of two between the values of reflectance factor measured at phase angles of 5° and 80° at the incidence angle i = 60°. Contrary to many other geologic samples, the JSC Mars-1 only shows a very limited increase of reflectance at phase angle > 100° (forward-scattering peak). The behavior of the curves in this region is one of the main sources of discrepancies between the measurements acquired with the four different instruments.

[46] The surface texture of the measured samples (roughness, compression, alignment of the grains…) is known to significantly affect their photometry [*Hapke*, 1993]. In order to assess the possible origin of the differences observed between measurements in Bloomsburg, Goddard, Grenoble, and Bern, we have measured with the PHIRE-2 instrument the photometry of four samples prepared from the same initial material but with four different preparation procedures (see Figure 1 and section 2.2).

[47] The three plots on the right of Figure 3 and the plots in Figure 4 show comparisons of the photometric properties measured for each of these four surfaces. While data plotted in Figure 3 are restricted to the principal plane to facilitate
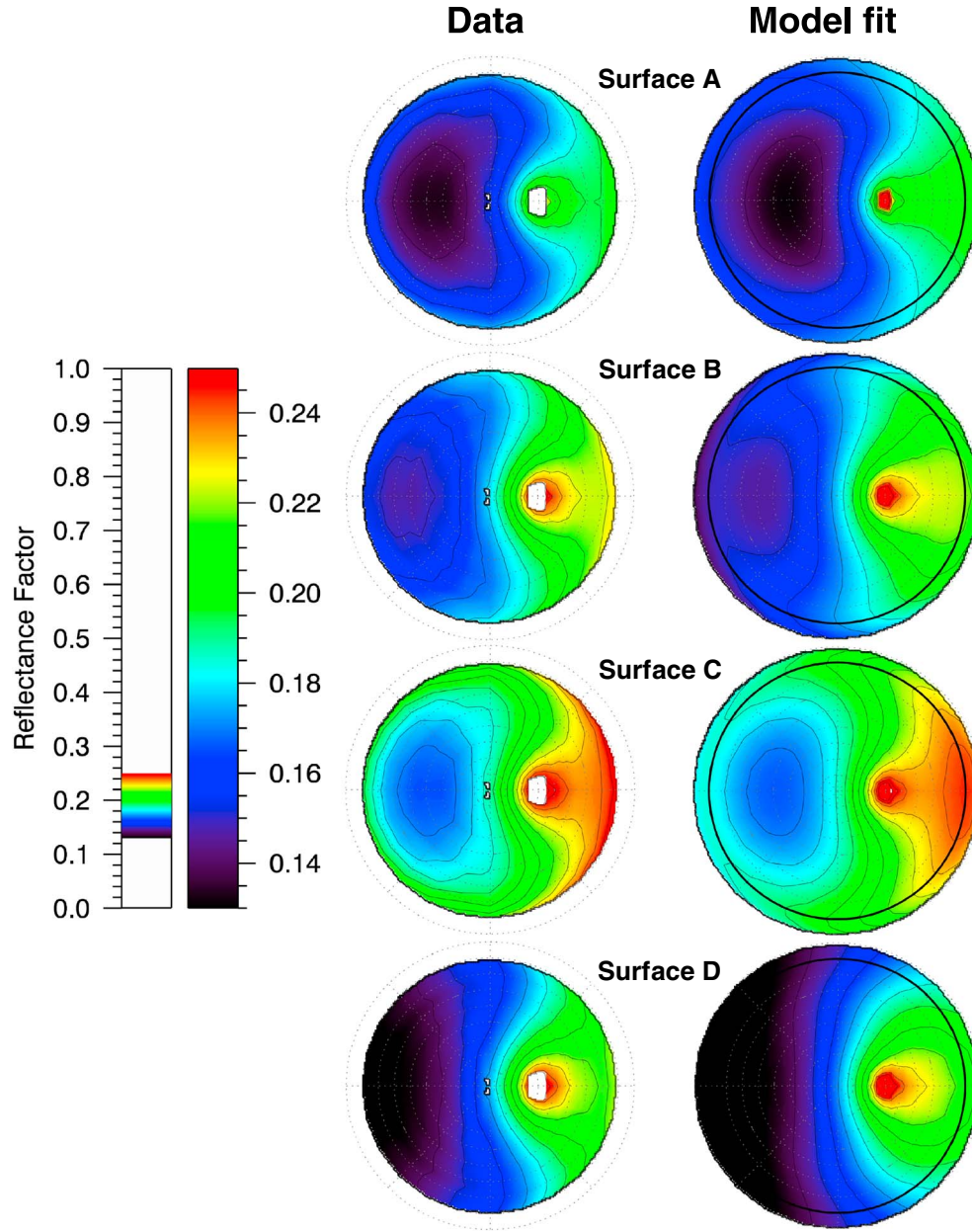
Figure 4. **Left**: reflectance factors measured with PHIRE-2 at a fixed wavelength: λ = 650 nm for the four different surfaces prepared with the JSC Mars-1 regolith simulant shown in Figure 1. Each of these plots displays the values of reflectance factor as a function of emission and azimuth angles, for a fixed incidence angle (i = 30°), following a rainbow color scale shown on the left. A double-colorbar is used to easily visualize both the absolute level of reflectance of the sample (left colorbar, fixed scale from 0 to 1) and the relative variations of reflectance inside a single plot (right colorbar, stretched between the minimum and maximum values of reflectance displayed in the polar plot). Faint dashed circles are iso-lines of emission angle, from 0° at the center, to 90° on the external circle. The direction of incident light is always on the right side of the diagrams, and apparent as a white "hole" corresponding to the area where measurements are not possible with the setup used (i.e., phase angles lower than 5°). The principal plane is the median horizontal line which separates the plot in two vertically mirrored half-disks. **Right**: corresponding reflectance values calculated from the Hapke coefficients obtained by fitting the Hapke photometric model to the measured data (provided in Table 1). Whereas data were only measured for emission angles between 5 and 80°, values can be calculated from the Hapke coefficients for any value of incidence, emission, and azimuth angle and complete (e = 0–90°) surfaces of reflectance factors are displayed.

Table 2. Same as Table 1 for Dry JSC Mars-1 Samples Measured on the BUG, Goddard, and IPAG Instruments (Figure 3)[a]

	ω	h_s	B_s	$\bar{\theta}$ (°)	b	c	χ^2_{red}
BUG	0.593	0.017	1.0	17.8	0.274	0.131	**1.2**
(670 nm)	(0.59, 0.60)	(0.01, 0.02)	(>0.77)	(17, 18)	(0.26, 0.28)	(0.08, 0.19)	
Goddard	0.542	0.062	0.932	12.1	0.168	1.109	**1.3**
(650 nm)	(0.52, 0.55)	(0.04, 0.21)	(>0.71)	(<15)	(0.12, 0.19)	(>0.93)	
IPAG	0.611	0.044	1.000	16.2	0.215	0.283	**0.9**
(680 nm)	(0.57, 0.63)	(0.01, 0.34)	(>0.17)	(12, 20)	(0.13, 0.28)	(−0.02, 0.66)	

[a]The wavelength ranges at which these measurements were obtained are slightly different: 670 nm (FWHM: 50 nm) for measurements in Bloomsburg (BUG), 650 nm (FWHM: 12 nm) for measurements in Goddard, and 680 nm (FWHM: 10 nm) for measurements in Grenoble. Measurements in Bern (PHIRE-2) for which Hapke parameters are reported in other tables were performed at a central wavelength of 650 nm (FWHM: 70 nm). These differences of wavelength ranges can result in minor vertical shifts of the curves but are unlikely to affect their shapes.

the quantitative comparison with data measured on the other instruments, Figure 4 also presents measurements obtained out of the principal plane, for a fixed incidence angle: i = 30° and a fixed wavelength: λ = 650 nm. Differences observed between samples A, B, C, and D (Figure 3, right column) are larger than between the four measurements obtained on different instruments (Figure 3, left column). It is striking that samples A and C on the one hand and B and D on the other hand show similar evolutions of the reflectance factor as a function of measurement geometry. However, there is a significant overall shift between values measured for samples A and C. Both samples A and C are smooth whereas samples B and D show significant roughness at the scale of the individual grain size. Smooth samples (A, C) show more pronounced increases of reflectance when the phase angle increases than rougher samples (B, D). We also note that the contrast in overall reflectance factor between the samples is more significant at low incidence angle (i = 0°, i = 30°) than at higher incidence (i = 60°). Tables 1 and 2 provide sets of Hapke parameters that allow reproducing all reflectance curves and surfaces displayed in Figures 3 and 4.

[48] If the JSC Mars-1 sample can be considered as a good analog for intermediate to high albedo red regions of Mars, many other regions show a much lower albedo and a dark grey color that, together with complementary spectral data sets [*Bandfield*, 2002; *Poulet et al.*, 2007], indicate a basaltic composition. As plausible analogs for the low-albedo regions, we have acquired photometric measurements on a more pristine basaltic sample, sorted in two different classes of particle size: 0–109 µm ("fine") and 109–1000 µm ("coarse"). Surfaces made out of these samples and individual grains for both size fractions are shown in Figure 2. The most notable difference when compared to the particles of JSC Mars-1 (Figure 1) is that many of the individual particles of the basalt sample appear relatively transparent when observed under the microscope whereas the particles of JSC Mars-1 appear opaque. This results in significant differences in the way the materials scatter visible light. In particular, Figure 5 shows that in addition to a pronounced backscattering peak, basalt samples also show a strong forward scattering. As a consequence and contrary to the JSC Mars-1 sample, the maximum of reflectance is observed in
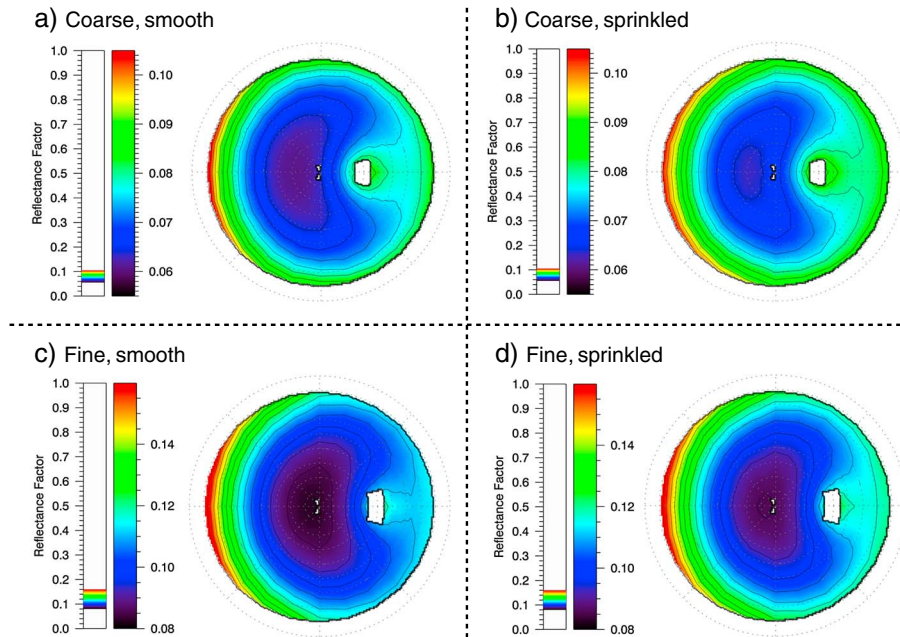
Figure 5. Comparison of the bidirectional reflectance factors of smooth (left column) and sprinkled (right column) surfaces prepared from (top row) coarse and (bottom row) fine fractions of the Hawaiian basaltic sand. All reflectance factors presented here were measured at a fixed incidence angle: i = 30° and a fixed wavelength: λ = 650 nm. See Figure 4 caption for additional explanations on how reflectance data are represented.

Table 3. Same as Table 1 for the Dry Basalts (Figure 5)

|	ω	h_s	B_s	$\bar{\theta}$ (°)	b	C	χ^2_{red}
Fine, smooth	0.474	0.029	1.0	15.7	0.30	−0.655	**5.6**
	(0.47, 0.48)	(0.02, 0.03)	(>0.98)	(15, 16)	(0.30, 0.31)	(−0.66, −0.65)	
Fine, sprinkled	0.478	0.026	1.0	15.2	0.295	−0.621	**4.9**
	(0.47, 0.48)	(0.02, 0.03)	(>0.97)	(15, 16)	(0.29, 0.30)	(−0.63, −0.62)	
Coarse, smooth	0.367	0.067	1.0	18.8	0.267	−0.60	**3.0**
	(0.36, 0.37)	(0.06, 0.08)	(>0.96)	(18, 19)	(0.26, 0.27)	(−0.61, −0.59)	
Coarse, sprinkled	0.368	0.077	1.0	18.8	0.244	−0.585	**3.0**
	(0.36, 0.37)	(0.07, 0.09)	(>0.98)	(18, 19)	(0.24, 0.25)	(−0.060, −0.058)	

the forward-scattering direction for basalt samples. The microtexture of the samples also appears very different. Whereas the basalt grains appear "clean" under the microscope, large grains of JSC Mars-1 sometimes seem to be covered by a material with finer grains and different color (Figure 1). It is thus probable that the size distribution of scatterers in JSC Mars-1 is shifted toward smaller scales compared to basaltic samples.

[49] We also note that the effects of particle size and surface texture (smooth versus sprinkled, see section 2.2.2) are very limited, consisting mostly in a general shift of the reflectance values by about 15% and contrasting with the behavior of JSC Mars-1 from which strong effects of the size of the particles and surface texture were observed. The transparency of the individual grains seems to be the prime parameter to explain the difference of observed behaviors between basalt samples and JSC Mars-1. Table 3 provides sets of Hapke parameters that allow reproducing all reflectance curves and surfaces displayed in Figure 5.

[50] Comparisons of reflectance measurements at different wavelengths reveal that the phase functions of all dry samples show a spectral dependence. Figure 6 illustrates this wavelength dependence by showing how spectral ratios calculated between near-infrared (905 and 750 for JSC Mars-1 and basalt, respectively) and short visible (450 nm) wavelengths vary with phase angle. The choice of a different wavelength (750 or 905 nm) for the near-infrared reflectance point was dictated by the observed difference in the spectra of the two samples, as the red slope extends further toward longer wavelength for JSC Mars-1 than for basalts.

[51] For all samples, the near-infrared / visible spectral ratios increase with phase angle up to about 80°. This behavior, observed for a variety of samples in the laboratory and a majority of rocky planetary surfaces, is known as phase reddening [e.g., *Schroder et al.*, 2011, *Beck et al.*, 2012; *Hapke et al.*, 2012; *Johnson et al.*, 2013]. At higher values of phase angle, the spectral ratio decreases for all JSC Mars-1 surfaces as well as the fine basalt surface but continues to increase for the coarse basalt surface. Similar behaviors were reported by *Johnson et al.* [2013] for surfaces prepared from JSC Mars-1 and surfaces prepared from analogs for lunar surfaces composed of crushed basalt. The same difference of behavior as the one reported here between the coarse and fine fractions of the Hawaii basalt is observed between the coarse (JSC-1 and JSC-1A) and fine (JSC-1AF) lunar simulant particle size fractions. The ratio phase curves for JSC Mars-1 (< 1 mm) reported by *Johnson et al.* [2013] are similar to the average phase curve

for all four surfaces prepared from JSC Mars-1 shown in Figure 6. *Johnson et al.* [2013] study in detail the spectral dependence of the Hapke parameters extracted from reflectance measurements of a variety of Martian and Lunar soil analogs. As our own results point to similar spectral behavior, we do not repeat this exercise here.
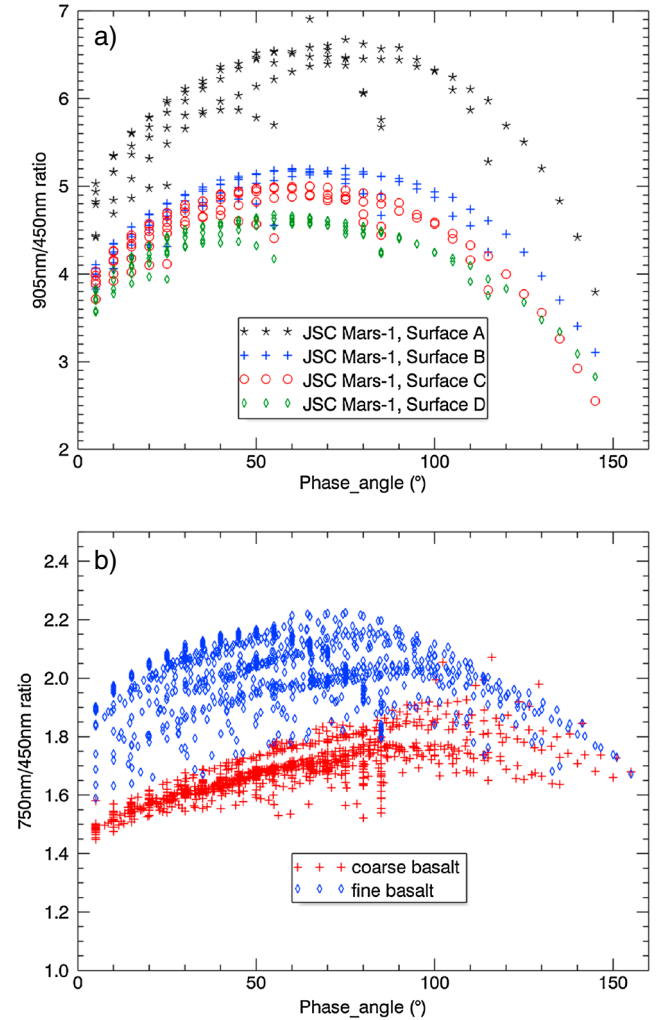
Figure 6. Near-infrared / visible spectral ratios plotted as a function of phase angle for (a) four different surfaces made of JSC Mars-1 and (b) two different surfaces (smooth) made of the coarse and fine fractions of basalt. The spectral ratios are calculated between wavelengths: 905 and 450 nm for the JSC Mars-1 samples and 750 and 450 nm for the basaltic sand samples.
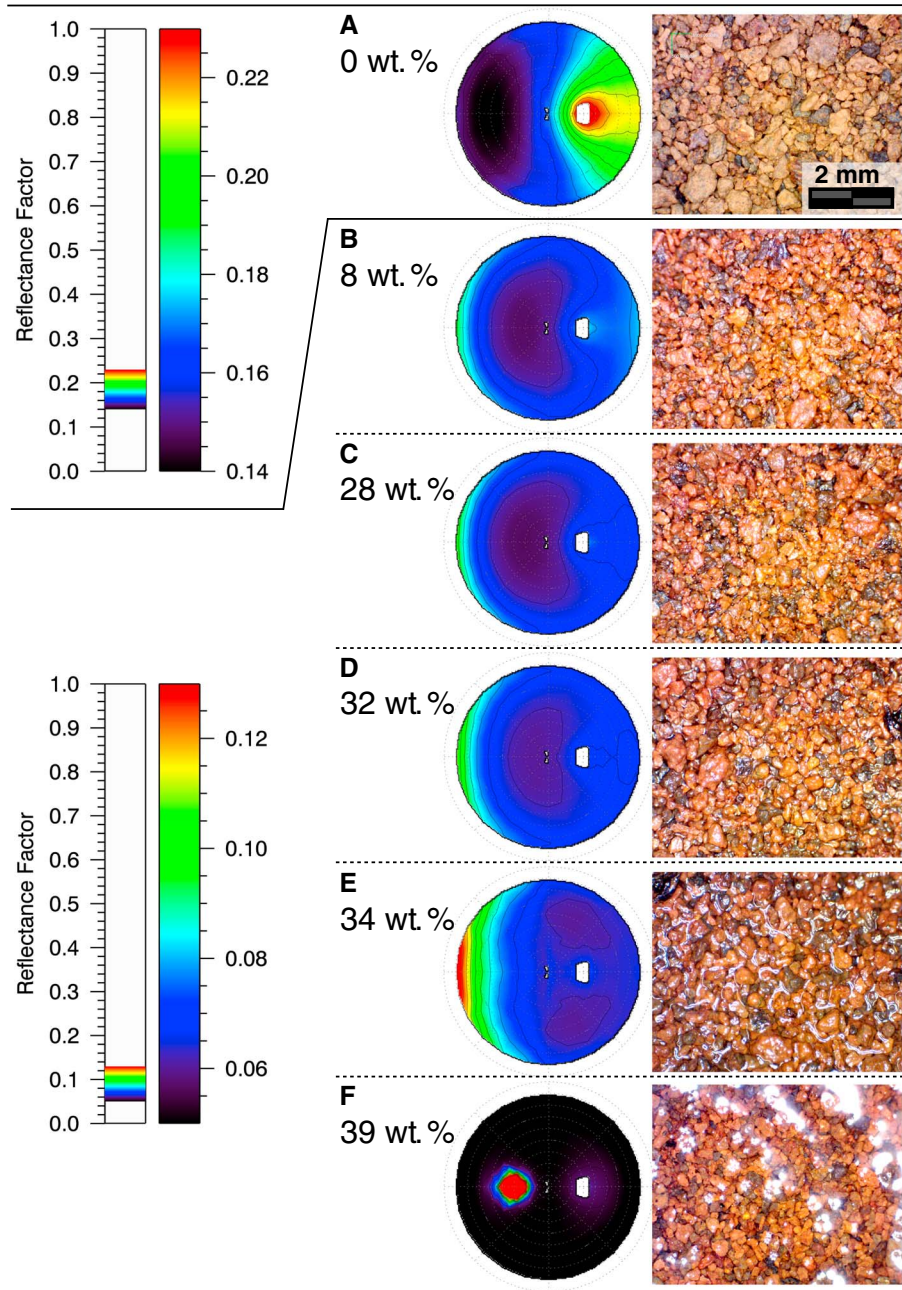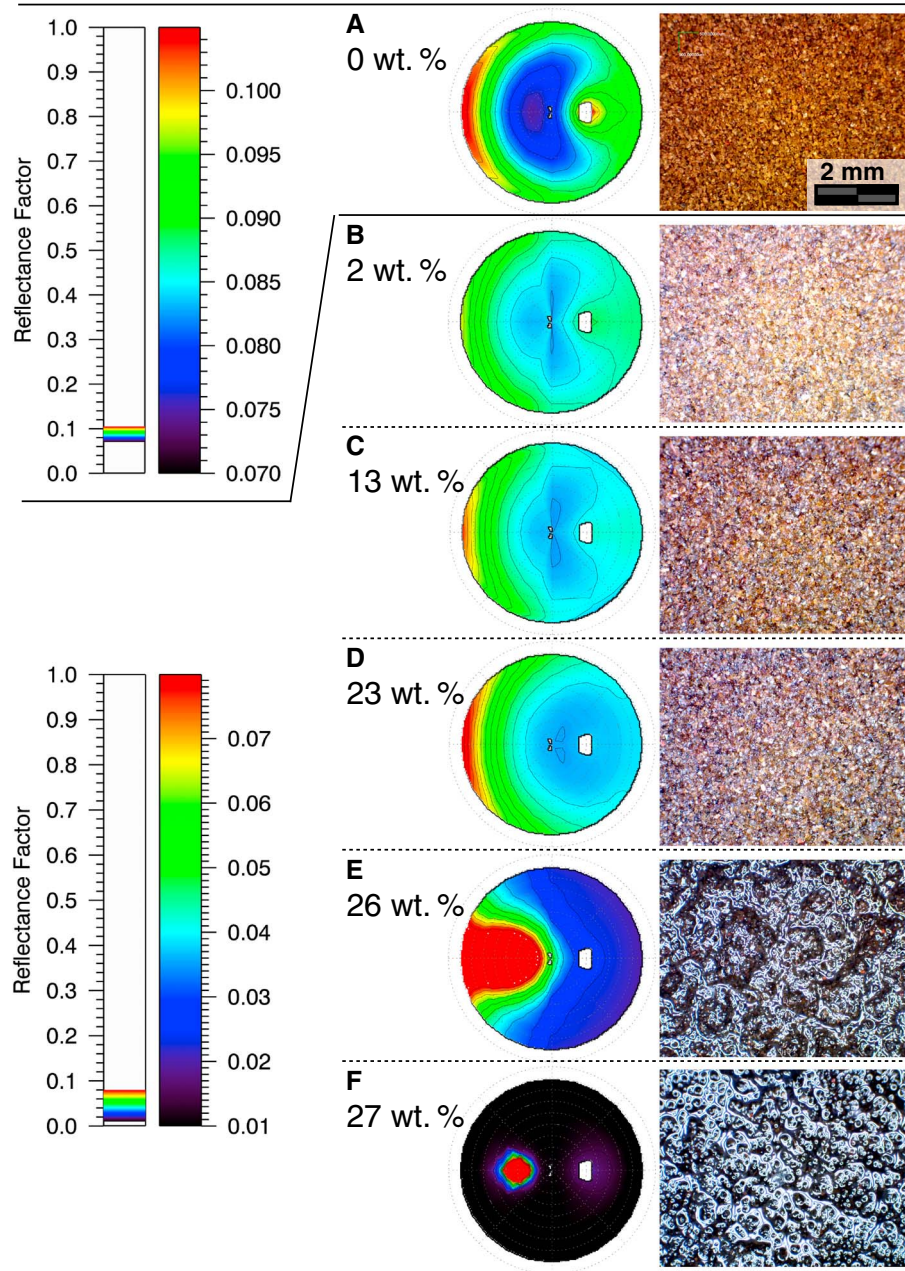
Figure 7. Left: Bidirectional reflectance factor at a fixed incidence angle of 30° and a fixed wavelength: $\lambda = 650$ nm plotted for dry and wet samples of JSC Mars-1 with different amounts of water. Right: optical microscope images of the samples surface. See Figure 4 caption for additional explanations on how reflectance data are represented. The colorbar on top corresponds to the dry surface (A) whereas the one on the bottom corresponds to all wet samples (B to F).

3.2. Wet Soils

[52] We conducted two types of experiments on three different samples to complement the pioneering study of *Gunderson et al.* [2007]. In the first type of experiments, increasing amounts of liquid water were sprayed incrementally onto samples initially prepared as surface B (Figure 1) until full water saturation (i.e., the entire pore space of the sample is filled by water, which starts to form a continuous thin film at the surface of the sample). At each step, the reflectance factor was measured for a single incidence angle: $i = 30°$ at a single wavelength: 650 nm. Microscope pictures were acquired before and after each of the photometric measurements. The mass of the sample was also systematically measured before and after each photometric measurement to calculate the bulk water content in weight percents (H_2O wt.%). However, because of vertical gradients of water concentration inside the thick samples, the value of bulk water content is likely to differ strongly from the value at the surface. This procedure was applied to the JSC Mars-1 sample and the two size fractions of the Hawaii basalt. Results are presented in Figures 7, 8, and 9, respectively.
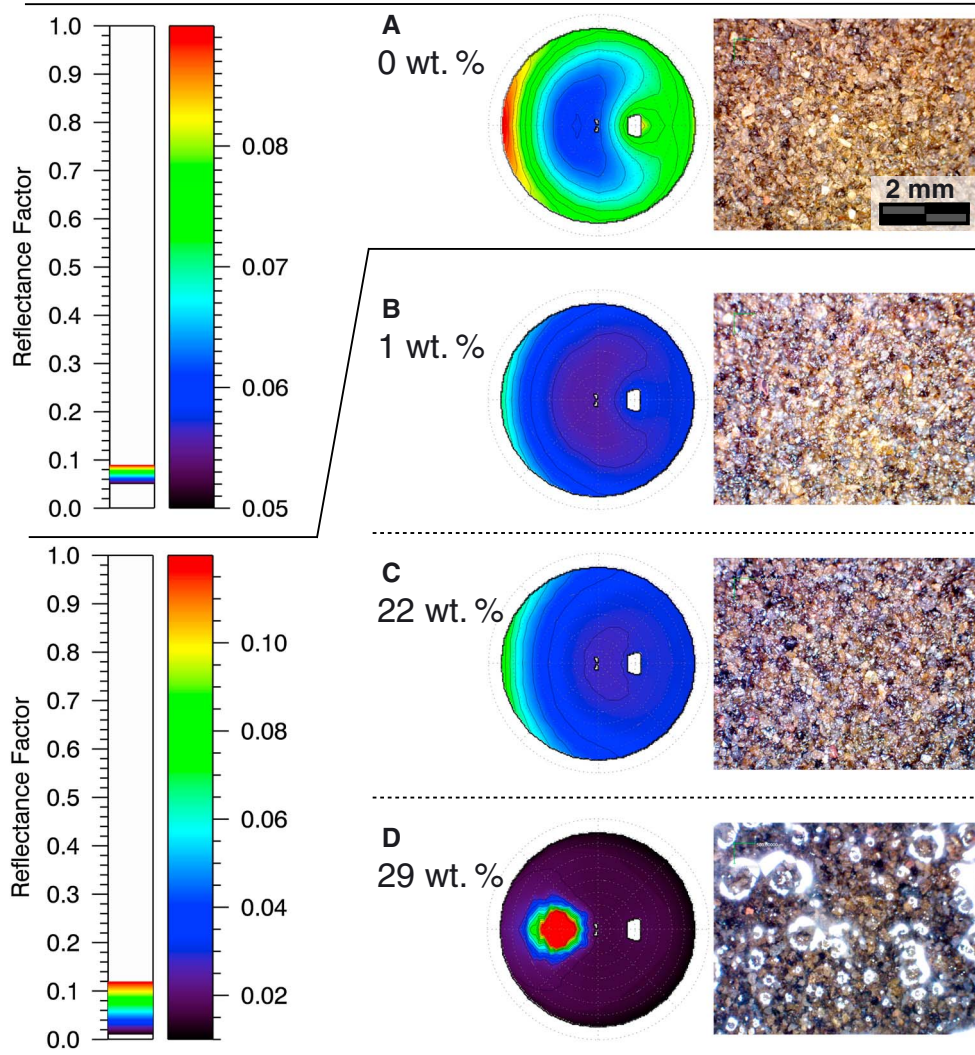
Figure 8. Left: Bidirectional reflectance factor at a fixed incidence angle of 30° and a fixed wavelength: $\lambda = 650$ nm plotted for dry and wet samples of the fine fraction of the Hawaiian basaltic sand with varying amounts of water. Right: optical microscope images of the samples surface. See Figure 4 caption for additional explanations on how reflectance data are represented. The colorbar on top corresponds to the dry surface (A) whereas the one on the bottom corresponds to all wet samples (B to F).

[53] The addition of liquid water results in similar evolution of the scattering properties for all samples. The backscattering peak rapidly decreases in amplitude when water is introduced and a strong forward-scattering peak progressively develops as the amount of water increases. The water first forms thin films around the grains. When meniscuses appear between the grains, the backscattering peak completely disappears and the forward-scattering peak becomes both extremely intense and very broad in emission and azimuth. When meniscuses join to produce a continuous film above surface grains, a very broad specular peak appears, superposed onto the forward-scattering peak. When the level of water is high enough to produce a horizontal film of water hiding the topography of the surface grains, the specular peak becomes much narrower and the forward-scattering peak disappears. The photometric behaviors described here appear similar to the ones reported by *Zhang and Voss* [2006] for most of their samples. They also observed a strong decrease of reflectance in the backscattering direction associated with an increase of reflectance in the forward-scattering direction for different types of artificial and natural samples, including Hawaiian dark beach sand that is potentially very similar to the Hawaiian sand we used.

Figure 9. Left: Bidirectional reflectance factor at a fixed incidence angle of 30° and a fixed wavelength: $\lambda = 650$ nm plotted for dry and wet samples of the coarse fraction of the Hawaiian basaltic sand with varying amounts of water. Right: optical microscope images of the samples surface. See Figure 4 caption for additional explanations on how reflectance data are represented. The colorbar on top corresponds to the dry surface (A) whereas the one on the bottom corresponds to all wet samples (B to D).

[54] Tables 4, 5, and 6 contain the Hapke coefficients obtained by fitting the photometric model to the measured data. In the case of JSC Mars-1, the reflectance data could be satisfactorily fitted by the model for the first three steps of wetting. For both the fine and coarse fraction of basalt, only the measurements for the two first steps could be fitted. When adding more water into the sample, the model was not able anymore to simulate the observed photometric behaviors, even before the appearance of the specular peak. Note than even if the model can be fitted to the data and Hapke parameters retrieved, one has to keep in mind that the wet surfaces studied here do not satisfy some of the hypotheses on which the model is based (independent scatterers). As a result, one should not try to interpret the coefficients

Table 4. Same as Table 1 for Three Wet JSC Mars-1 Samples as Well as the Initial Dry Surface (Figure 7)

	ω	h_s	B_s	$\bar{\theta}$ (°)	b	C	χ^2_{red}
Dry	0.567	0.029	1.0	20.5	0.235	0.413	**0.7**
	(0.56, 0.57)	(0.02, 0.09)	(>0.63)	(20, 21)	(0.21, 0.25)	(0.34, 0.50)	
Wet0	0.364	0.013	1.0	21.6	0.301	−0.508	**0.9**
	(0.36, 0.37)	(0.01, 0.05)	(>0.41)	(21, 22)	(0.29, 0.31)	(−0.53, −0.48)	
Wet1	0.382	0.006	1.0	24.4	0.330	−0.604	**3.1**
	(0.38, 0.39)	(<0.05)	(>0.19)	(24–25)	(0.32, 0.34)	(−0.63, −0.58)	
Wet2	0.412	0.001	0.558	26.6	0.346	−0.682	**5.8**
	(0.41, 0.42)	(-)	(-)	(26, 27)	(0.33, 0.36)	(−0.70, −0.66)	

Table 5. Same as Table 1 for Two Wet Fine Basalt Samples as Well as the Initial Dry Surface (Figure 8)

	ω	h_s	B_s	$\bar{\theta}$ (°)	b	c	χ^2_{red}
Dry	0.416	0.092	0.904	25.8	0.218	−0.581	**3.5**
	(0.40, 0.43)	(0.04, 0.18)	(>0.72)	(25, 26)	(0.19, 0.24)	(−0.66, −0.52)	
Wet0	0.274	0.053	0.603	26.6	0.301	−0.741	**5.2**
	(0.26, 0.28)	(0.02, 0.17)	(>0.42)	(26, 27)	(0.28, 0.32)	(−0.79, −0.72)	
Wet1	0.305	0.014	0.818	26.3	0.366	−0.834	**4.2**
	(0.30, 0.31)	(0.01, 0.13)	(>0.27)	(26, 27)	(0.35, 0.38)	(−0.85, −0.82)	

provided in Tables 4, 5, and 6 in terms of physical properties but only use them to reproduce the measured behaviors or extrapolate them to other geometries.

[55] A second type of experiment was carried out with the JSC Mars-1 sample only. The sample was first saturated with water and then left to dry while photometric measurements were acquired. The sample was removed from the PHIRE-2 instrument between successive sequences of measurements to take pictures of the surface with the microscope. Because the sample was drying very slowly, it was possible to obtain more complete measurements. In addition to the incidence angle i = 30° as in previous experiments, the reflectance factors have also been measured at incidence angles of i = 0° and i = 60°. Measurements in the principal plane were also acquired at six different wavelengths: 450, 550, 650, 750, 905, and 1064 nm.

[56] Figure 10 shows the reflectance factors measured in the principal plane for the drying JSC Mars-1 at the three different incidence angles: i = 0°, 30°, and 60°. The forward-scattering peak is much more intense and narrower at i = 60° than at i = 30°. At i = 0°, a moderate increase of reflectance toward low phase angle might be caused by specular reflection from water as no backscattering is observed at i = 30° and i = 60°.

[57] A comparison of the visible spectra of the various wet JSC Mars-1 surfaces as well as the dry surfaces before and after the experiment is shown in Figure 11. All spectra were produced from values of reflectance factor measured at i = 0° and e = 30° for each wavelength. At such a low spectral resolution, the only prominent spectral feature is the very steep red slope between 450 and 750 nm. This slope is strongly reduced by the introduction of water into the sample. This causes the loss of the red color in the wet sample that is also observable by eye. It is also interesting to note that in this low-phase angle geometry, the values of reflectance factors for the wet samples only show very limited evolution with time. In other words, the sample appears as dark at the end of the drying sequence, just before the last thin films of water disappear, as they appear at the beginning of the drying sequence, when the sample is completely saturated with water, and about three times darker than the dry samples.

The wet samples even appear slightly darker when they are not saturated in water anymore because of the disappearance of the broad specular peak that shows its influence up to phase angles of about 30°.

[58] Ratios between values of reflectance factors measured in different geometries ("spectral ratios") show significant evolution with measurement geometry, as illustrated in Figure 12. The visible spectral ratio (Figure 12a), calculated as: VIS = REFF(750 nm) / REFF(450 nm), where REFF(λ) is the reflectance factor at the wavelength λ, is a measure of the steepness of the red slope. The near-infrared spectral ratio (Figure 12b), calculated as: NIR = REFF(750 nm) / REFF(1064 nm), is potentially affected by the weak absorption of H_2O above 1 μm.

[59] The VIS spectral ratio is strongly affected by the amount of water in the sample, in a way that is highly dependent on the measurement geometry. While this spectral criterion is nearly constant, between 4 and 5, for the dry sample, it shows a strong evolution with emission angle for all wet samples with a strong decrease at large positive emission angles and a strong increase at large negative emission angles. This evolution of the VIS spectral ratio for wet samples mimics the one of reflectance in general: the spectral slope is steeper where the overall reflectance is low and is shallower where the reflectance is high (forward-scattering direction or specular position).
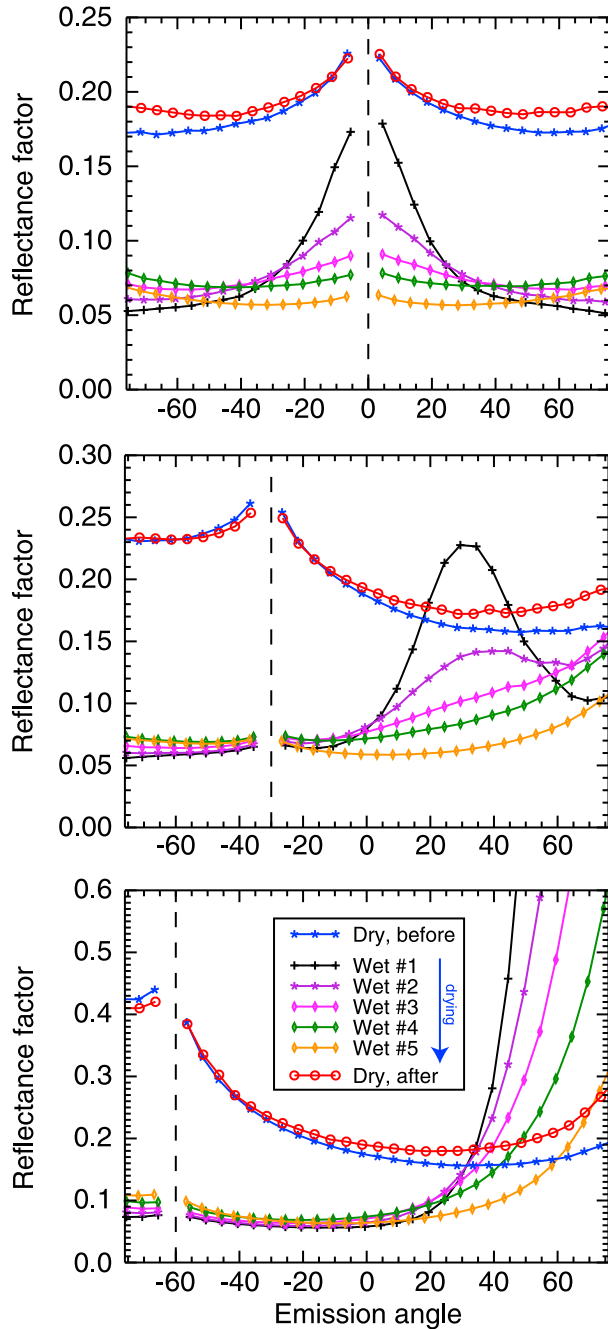
[60] The NIR ratio shows less dependence to the measurement geometry than the VIS ratio. It slightly increases in the specular position for samples that show a specular reflection as a result of absorption by water at 1064 nm. In the case of the dry sample, the linear decrease of the NIR ratio when the emission angle increases is the expression of the phase reddening (see section 3.1 and [*Johnson et al.*, 2013]).

[61] We compare in Figure 13 the reflectance factors of dry JSC Mars-1 surfaces, before spraying water on it and after it has completely dried out. The Hapke coefficients retrieved by fitting the photometric model to the measured reflectance data for the dried JSC Mars-1 surface are provided in Table 7. After drying, the surface shows an overall higher reflectance in all geometries than in its initial state. In addition, a significant forward-scattering peak has developed, which

Table 6. Same as Table 1 for Two Wet Coarse Basalt Samples as Well as the Initial Dry Surface (Figure 9)

|	ω	h_s	B_s	$\bar{\theta}$ (°)	b	c	χ^2_{red}
Dry	0.363	0.056	0.772	24.2	0.252	−0.557	**1.8**
	(0.35, 0.37)	(0.02, 0.15)	(>0.58)	(24, 25)	(0.23, 0.27)	(−0.63, −0.52)	
Wet0	0.327	1.0	0.001	23.7	0.576	−0.946	**2.8**
	(0.22, 0.34)	(-)	(-)	(23, 24)	(0.56, 0.60)	(−0.95, −0.94)	
Wet1	0.334	1.0	0.001	23.2	0.582	−0.947	**2.3**
	(0.33, 0.34)	(-)	(-)	(23, 24)	(0.55, 0.59)	(−0.95, −0.94)	

Figure 10. Bidirectional reflectance factors in the principal plane measured during drying of the JSC Mars-1 sample. Incidence angle = (top) 0°, (middle) 30°, and (bottom) 60°. Wavelength: λ = 650 nm. Measurements were performed for five successive steps of a drying sequence (step #1 to step #5) in addition to the dry states before and after the wetting and drying sequence (step #1 corresponds to the maximum of water in the sample).
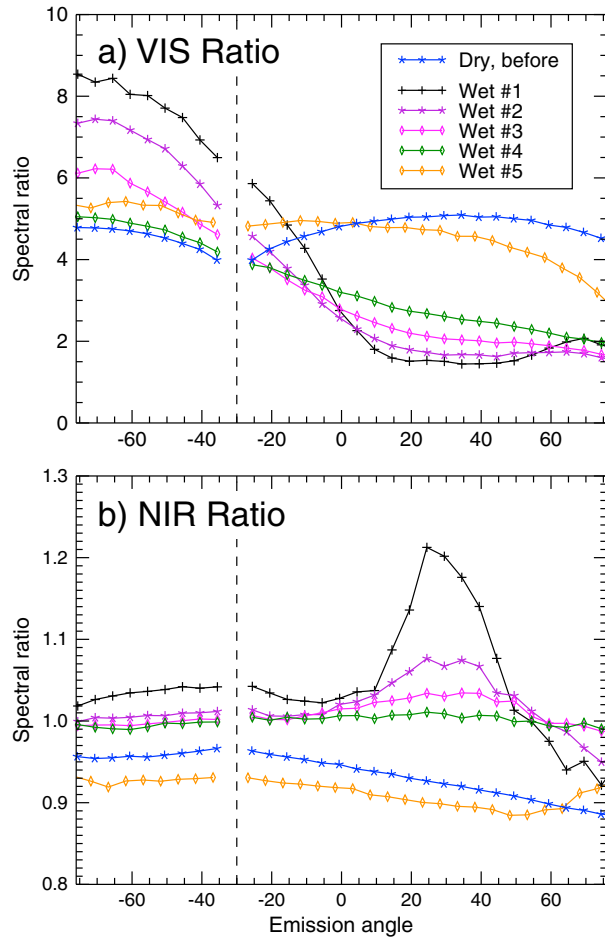
the grains. The first layer of grains at the surface even shows some cohesion. It forms a very thin crust that is locally disrupted to reveal underlying "cavities" with the dimension of a few grains, which appear dark on the images. Two examples of such features can be seen on the right picture in Figure 13.

[62] It is interesting to compare the result of this experiment with the results reported in section 3.1 for dry samples prepared with different procedures. In particular, Figure 4 shows the same variability of photometry between samples A and C on the one hand and B and D on the other hand as for the JSC Mars-1 sample before and after spraying water on it. Samples A and C were prepared with smooth surfaces whereas samples B and D where rough. This confirms the influence of the microscopic roughness on the photometric properties of the dried sample.

[63] In the context of possible current emissions of liquid water at Mars surface, another factor that might have a strong influence on the photometry has to be considered: the presence of dissolved salts in the water. We have conducted a single simple experiment to study the effects of the crystallization of sodium chloride salt on the reflectance of a dried coarse basalt sample. Figure 14 shows a microscope picture of the dried basalt sample, with an incomplete crust of salt at its surface. The Hapke coefficients retrieved by fitting the photometric model to the measured reflectance data for this surface are provided in Table 7. The development of the salt crust results in significant photometric changes, compared to the initial dry state (Figure 5). The most drastic effect is the strong increase of the reflectance at all geometries caused by the much higher single scattering albedo of the sodium chloride crystals compared to basalt grains. However, the general shape of the scattering function is also considerably modified: the significant forward-scattering peak shown by the pure basalt samples is largely reduced and maxima of reflectance are observed at moderate phase angle, on the backward scattering side.
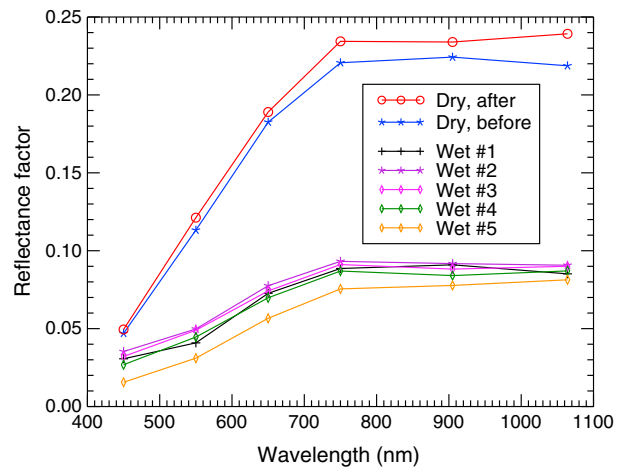
Figure 11. Visible – NIR bidirectional reflectance spectra of the drying JSC Mars-1 sample at different time steps measured for vertical incidence: i = 0° and emission: e = 30°. Measurements were performed for five successive steps of a drying sequence (step #1 to step #5) in addition to the dry states before and after the wetting and drying sequence (step #1 corresponds to the maximum of water in the sample).

was completely absent in the initial sample. Close examination of the microscope pictures reveals the origin of the observed photometric variability. While the initial sample, produced by spraying the powder, shows a high microscopic roughness and a random orientation of the grains, the sample that has been wet shows a much smoother surface as a result of a preferential horizontal orientation of

Figure 12. Relationships between spectral ratios and emission angle for the drying JSC Mars-1 sample at different time steps. (a) The VIS ratio (750/450 nm) represents the steepness of the visible ref slope between 450 and 750 nm. (b) The NIR ratio (750/1064 nm) is affected by the water absorption at 1 μm. Measurements were performed for five successive steps of a drying sequence (step #1 to step #5) in addition to the dry state before wetting (step #1 corresponds to the maximum of water in the sample).

3.3. Ground Ice and Frost on Ground

[64] The different procedures used to prepare "icy soils" (see Methods Section) produced samples that show strongly contrasted photometric behaviors. The reflectance factors measured at a single incidence angle i = 30° for three different samples of ice-bearing JSC Mars-1 (samples: "frozen" A, B, and C) and for the dry initial state are compared in Figure 15. As for dry and wet samples, microscope images of the icy samples provide clues to understand their macroscopic photometric behaviors.

[65] Most of the icy samples that we prepared show a specular reflection of variable intensity. Sample "frozen A," prepared by leaving a wet JSC Mars-1 sample to freeze at −30°C, consists of a matrix of ice around the grains in the bulk of the samples. However, at the surface, the upper parts of the top grains appear free of ice. As in the ice-free sample, no forward-scattering peak can be observed. However, the maximum of reflectance is no longer in the backward direction but

at higher emission angle on the backward scattering side, similar to what was observed for the basalt sample with a crust of salt (Figure 14). A weak specular reflection is also observed.

[66] Albeit the bulk of sample "frozen B" is similar to the one of "frozen A," a thin layer of ice covers the entire surface, following the topography of the underlying grains (Figure 15). The presence of this conformal film of water ice on the surfaces results in a pronounced forward-scattering behavior and the presence of a specular peak of a lower intensity. This behavior was also observed for wet samples. However, the photometry of sample "frozen B" strongly differs from the one of wet samples at high emission angle, in the backward and sideward directions. Indeed, sample "frozen B" shows increasing reflectance with emission angle in these directions, contrary to all wet samples. Increasing the thickness of the transparent ice film results in a loss of the surface roughness which causes the disappearance of the forward-scattering peak and the development of an intense and narrow specular peak (sample "frozen C" prepared from JSC Mars-1 in Figure 15). These drastic changes in the shape of the phase function result in the fact that frozen samples appear darker than dry samples at low to intermediate phase angles and brighter than dry samples around the specular geometry as well as at high phase angles as long as the ice film remains thin enough to preserve the topography of the underlying grains.

[67] The photometric effect of fine frost deposited on the surface of the grains (example of JSC Mars-1 in Figure 16) strongly differs from all cases of icy samples described before. Because the sublimation was taking place very rapidly at a temperature of 253 K, we had to restrict our measurements to the principal plane for one fixed incidence angle and one fixed wavelength to capture the temporal evolution with a time resolution of about 3 min. The effect of frost on the reflectance factors measured at an incidence angle: i = 30° is presented in Figure 17 and Table 7 provides the Hapke parameters obtained by fitting the photometric model to all curves shown in Figure 17. The presence of frost on the surface of the grains moderately increases the reflectance factor at all geometries but its most prominent effect is to produce an intense forward-scattering peak.

4. Discussion

4.1. Results of Data Fitting by the Hapke Model

[68] Most of the measurements presented in the Results section were satisfactorily fitted by the Hapke photometric model and sets of parameters corresponding to data shown in the figures were provided in Tables 1 to 8. It is particularly interesting to note the good agreement between the sets of Hapke coefficients that we have obtained using the BUG data for the JSC Mars-1 sample and that *Johnson et al.* [2013] have obtained from the same data but using a different fitting procedure, both in terms of best fit values and ranges of uncertainties. Albeit our initial objective with data fitting was to provide sets of coefficients that can be used to easily reproduce, extrapolate, and compare our data, we also determined the ranges of uncertainty on the determination of each of these parameters to allow interested readers to go further in the interpretation of these coefficients. Not surprisingly, the parameters are better constraint when the number and diversity of measurement geometries are the highest (for dry samples) and can be severely under-constraint when
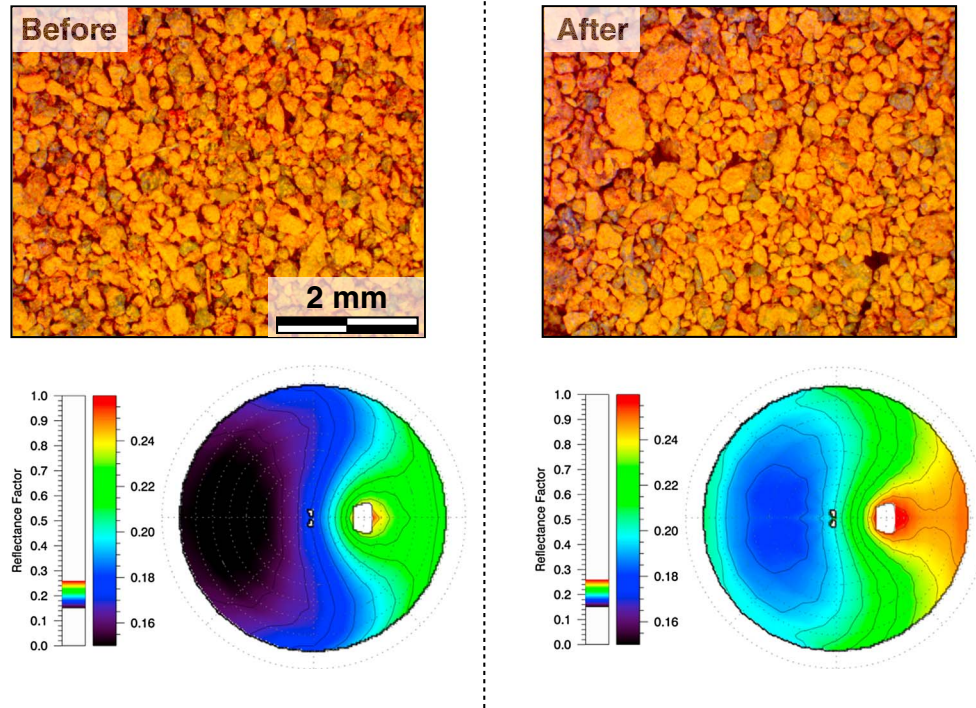
Figure 13. Comparison of the surface of the JSC Mars-1 sample (left column) before and (right column) after a wetting and drying sequence as observed under the (top) optical microscope and by bidirectional reflectance measurements at a fixed incidence angle: i = 30° and a fixed wavelength: λ = 650 nm. See Figure 4 caption for additional explanations on how reflectance data are represented.

measurements had to be restricted to one unique incidence angle and/or the principal plane.

[69] Figure 18 offers a good summary of some of the Hapke parameters retrieved, in the form of the classical "Hockey stick" plot in which values of the b coefficient (width of the scattering lobe) are plotted as a function of the c coefficient values (backscattering fraction). Error bars corresponding to the uncertainty ranges reported in Tables 1 to 8 are displayed to help visualizing the significance of the observed differences between points. The "Hockey stick" empirical relation, established by *Hapke* [2012] on the basis of many measured data sets, is shown as a dashed line. Note that this relation is not a single line but has a certain width around the central line. The significance of the shape of the central line and the width of the distribution are both discussed by *Hapke* [2012] and physical interpretations of these observations are proposed. The dry and wet samples measured in this study (Figure 18a) fall close to the central line, slightly shifted to the left for points with negative values of the c coefficient.

[70] Some of the well-known weaknesses in using the Hapke photometric model to interpret measured reflectance data are immediately visible on Figure 18. The most obvious is the wide spread in c values (and to a lower extent in b values)
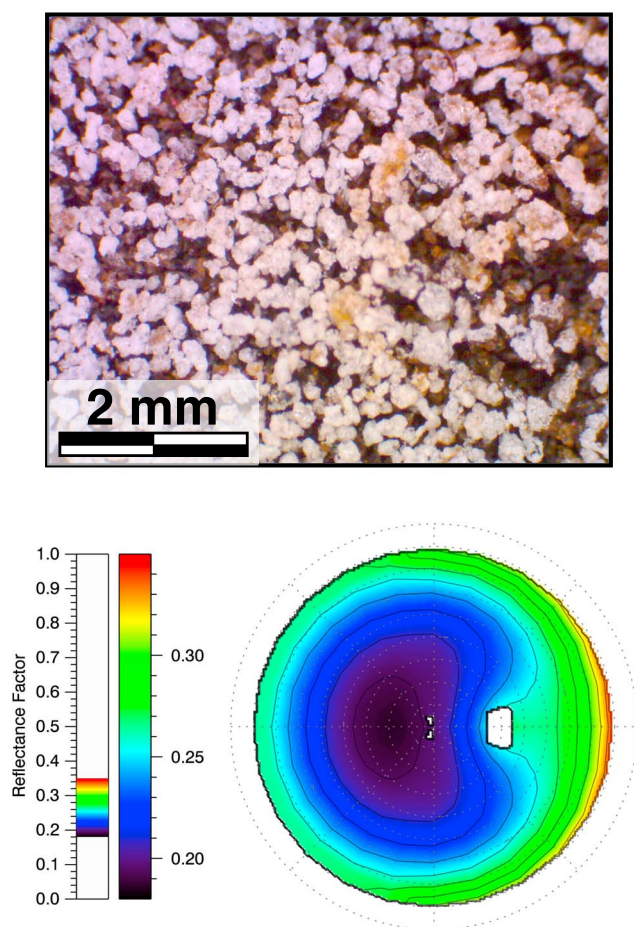
for the various surfaces prepared from similar JSC Mars-1 powder. As b and c are describing the scattering behaviors of the individual particles that compose the surface, they should not be influenced by macroscopic parameters such as roughness and compaction. Note that surfaces B and D, prepared as rougher surfaces, also show slightly higher values of $\overline{\theta}$ than surfaces A and C (16–18° vs. 13–15°, respectively). Part of the difference of roughness was thus correctly ascribed to the macroscopic roughness parameter $\overline{\theta}$ but another significant part was incorrectly ascribed to the scattering properties of individual particles. One could also wonder about the physical significance of the Hockey stick relation after noticing that the wet samples apparently lie on the same Hockey stick line as the dry samples, although the physics of light scattering by wet samples is not supposed to be reproduced correctly by the model.

[71] The Hapke photometric model is an invaluable tool for the analysis and interpretation of measured reflectance data. Unfortunately, the ability of the model to invert measured data to retrieve physical properties of the samples seems to remain limited, not necessarily because of deficiencies in the model itself but because of the complexity of the particulate medium and the light scattering process, in

Table 7. Same as Table 1 for the Dried Surface of JSC Mars-1 Shown in Figure 13 (After Wetting/Drying) and the Dried Surface of Coarse Basalt Covered by a Crust of Salt Shown in Figure 14

	ω	h_s	B_s	$\overline{\theta}$ (°)	b	c	χ^2_{red}
Dried JSC Mars-1	0.641	0.024	1.0	18.8	0.197	0.449	**4.9**
	(0.64, 0.65)	(0.02, 0.03)	(>0.87)	(18, 19)	(0.19, 0.20)	(0.42, 0.49)	
Basalt + saltcrust	0.633	0.293	1.0	0	0.002	1.256	**2.3**
	(0.63, 0.64)	(0.29, 0.34)	(>0.99)	(<4)	(<0.04)	(-)	

Figure 14. Top: optical microscope picture of the surface of a sample resulting from the drying of coarse basalt previously wetted by a saturated solution of NaCl. A crust of salt has formed at the surface of the sample. The size of the salt grains is comparable to the size of the basalt grains. Bottom: bidirectional reflectance measurements of the surface shown on top at a fixed incidence angle: $i = 30°$ and a fixed wavelength: $\lambda = 650$ nm. See Figure 4 caption for additional explanations on how reflectance data are represented.

particular the fact that different properties of a surface might have similar influences on its reflectance. Because the physical interpretation of the different coefficients retrieved from fitting the model to the data currently remains elusive, the rest of the discussion will use direct descriptions of the reflectance curves and surfaces and avoid direct comparisons between Hapke's coefficients. Figure 19 summarizes all the photometric behaviors described in the Results Section by showing how different properties of the sample influence different areas of the surface defined by the bidirectional reflectance values. The trends illustrated in Figure 19 will be discussed in the following subsection with a particular emphasis on their implications for optical observations of the Martian surface.

4.2. On the Photometry of Dry Surfaces on Mars

[72] The comparison of photometric measurements acquired on dry Martian analogs in this work and in previous studies allows us to draw conclusions about what we can expect for the surface of Mars. A dominant backward scattering behavior is observed for all plausible geologic analogs, independent of the method used to prepare the surface. A backscattering behavior should thus be dominant everywhere on the surface of Mars, both in bright and dark regions. This has significant implications for the calibration of remote-sensing data sets as results show that relative differences of up to 25% are expected between measurements of reflectance at near-zero phase angles and at phase angles of a few tens of degrees. Mosaicking of data with the assumption of a Lambertian behavior of the surface would thus result in significant photometric mismatches. Time series consisting of observations of a fixed region observed at different seasons, and thus different solar incidence angles, can also be biased by this non-Lambertian behavior. Numerous evidences for this non-Lambertian behavior have been collected during the calibration and mosaicking of different imaging data sets [*Kirk et al.*, 1999; *Geissler*, 2005; *Johnson et al.*, 2008].

[73] In addition to the dominant backscattering behavior, we can expect a slight forward-scattering peak to be present on different types of terrains. In particular, it seems that dark basaltic surfaces show a significant forward scattering, even with relatively coarse grains. It should thus be possible to observe forward scattering over surfaces covered by basaltic sand on Mars. Contamination of these surfaces by fine red dust might result in a strong decrease of the forward-scattering peak. As a consequence, the intensity of the forward-scattering peak could be used as a qualitative indicator of dust contamination. This forward scattering will only be significant at high phase angles ($> 100°$) that are rarely reached in standard remote-sensing observations from orbit, but readily seen from the ground.

[74] There are other conditions in which a forward-scattering peak can be observed, even with a large amount of fine red material. Comparison of the photometry of various samples prepared in different ways with JSC Mars-1 clearly shows that a forward-scattering peak at high phase angle can be observed with smooth surfaces but is inhibited when the surface is rough at the millimeter or submillimeter scale. *Johnson et al.* [2013] and *Pommerol and Schmitt* [2008] had previously shown similar effects with other materials. The presence of boulders on the surface, unresolved on the images, will result in the appearance of shadows that will also reduce the apparent reflectance measured at high phase angles. As a result, it should be possible to observe forward-scattering peaks on Mars, over terrains that are smooth at all spatial scales, from submillimeter to meters.

[75] In situ and orbital optical observations of the Martian surface have already been analyzed by a number of researchers in order to determine the bidirectional reflectance properties of various types of terrain. A global average phase curve of Mars surface was recently derived by *Vincendon* [2013] using orbital OMEGA and CRISM data. *Fernando et al.* [2013] have also retrieved the bidirectional reflectance of a number of regions of interest at both Spirit and Opportunity landing sites from CRISM observations. At the surface, in situ observations by the Spirit and Opportunity rovers have been analyzed to retrieve bidirectional reflectance properties. Hapke coefficients have been computed for each of these observations. Rather than directly comparing the values of these coefficients, we used them to calculate reflectance values in the same geometries as our lab measurements. We
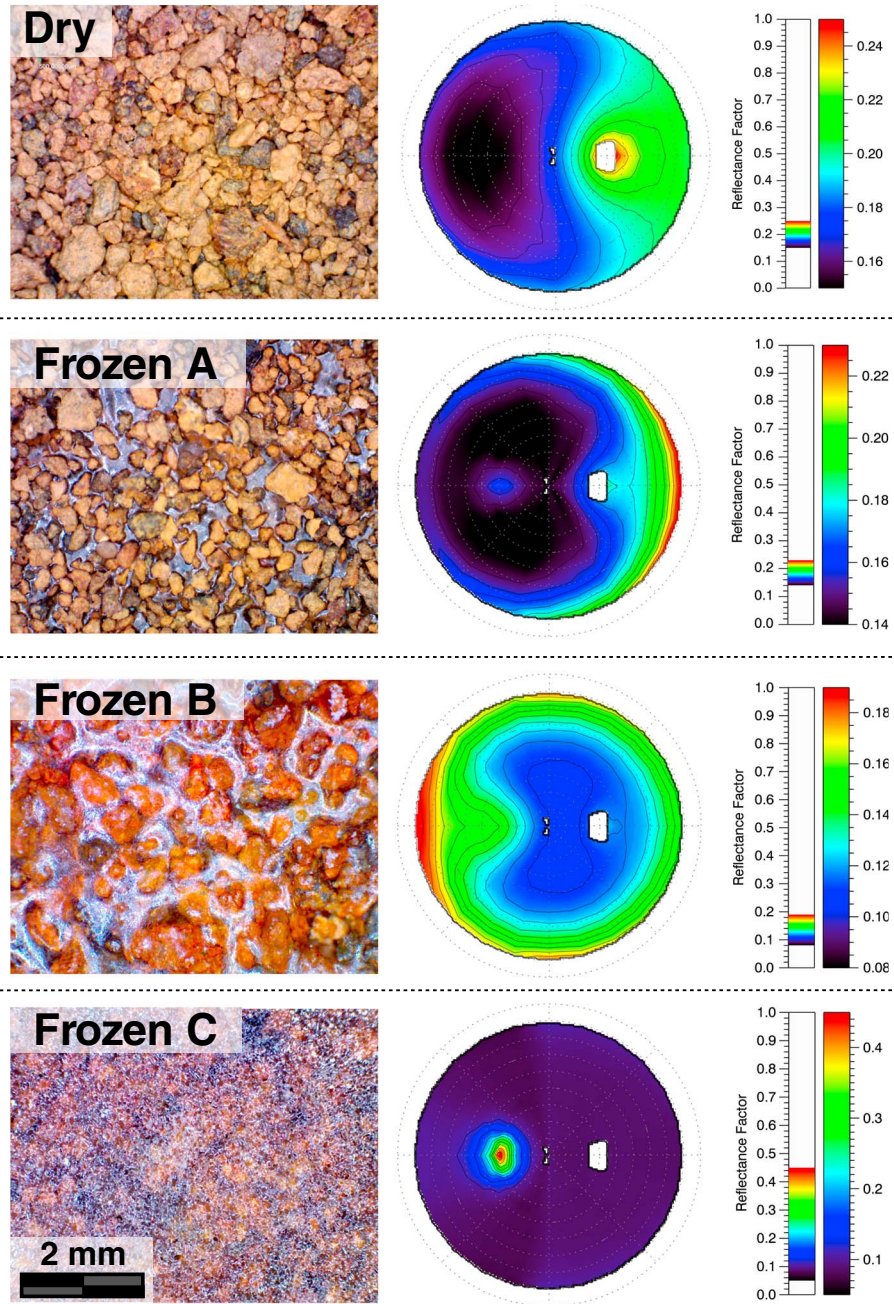
Figure 15. (Left) Microscope pictures and (right) photometric measurements at the incidence angle: i = 30° and wavelength: λ = 650 nm for three different samples of ice-bearing JSC Mars-1 ("Frozen A," "Frozen B," "Frozen C") and one sample of ice-free JSC Mars-1 ("dry," surface type B, see Figure 4). See Figure 4 caption for additional explanations on how reflectance data are represented and section 2.2.4 for descriptions of the samples preparation.

calculated "surfaces" or reflectance factors for an incidence angle of 30°, similar to the ones shown in Figures 4 and 5, 7 to 9, and 13 to 15. For both Mars observations and laboratory measurements, we have calculated and averaged different reflectance values from different sets of Hapke parameters corresponding to similar regions of interest (CRISM orbital observations), classes of terrain or features (PANCAM in situ observations), or material (laboratory experiments). Averaging reflectance factor values corresponds to simulating a geographic (subpixel) mixture.

[76] The contrast of average photometric behaviors observed in situ on Mars between soils and grey rocks is reproduced to some extent by the contrast of behaviors between JSC Mars-1 and basalt samples evidenced in laboratory measurements. Grey rocks in Gusev show maxima of reflectance at high phase angle in the forward-scattering direction, as basalt samples measured in the laboratory, whereas soils in Gusev and Meridiani show clear maxima of reflectance in the backscattering direction, as the JSC Mars-1 samples. Soils in Gusev and, to a lower extent, in Meridiani also show an increase of
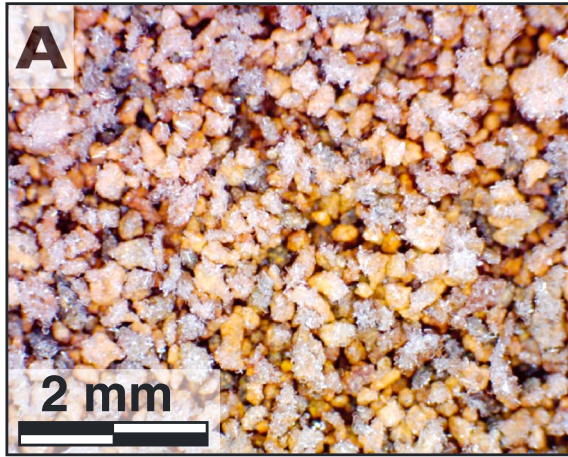
Figure 16. Microscope picture (6 × 5 mm) of a frosted JSC Mars-1 sample, prior to its introduction in the freezer for photometric measurements. The JSC Mars-1 sample, which also contains water ice in its bulk which is not visible on the picture, was previously kept at a temperature of 243 K for hours, then exposed to ambient laboratory conditions (293 K), resulting in a condensation of fine water frost at the surface of the grains from atmospheric water vapor.

reflectance in the forward-scattering direction, which looks closer to what is observed with the smoother JSC Mars-1 surfaces (A and C, Figure 4) than with the rougher surfaces (B and D). The orbital observations, however, show an opposite trend with more pronounced scattering in the forward direction in Meridiani than in Gusev. Finally, the global average photometric behavior derived by *Vincendon* [2013] from both OMEGA and CRISM data looks relatively similar to the average JSC Mars-1 behavior shown in Figure 20. Because the relative areal fractions of the different types of terrains observed in situ and averaged in a single CRISM or OMEGA pixel are not known, it remains difficult to establish relation between in situ and orbital observations and even more challenging between laboratory samples and orbital observations. Future multi-instrumental analyses combining multiangular observations, high-resolution imaging, and high-resolution topography will be necessary to make the link between observations and measurements at such different spatial scales.

[77] The spectral dependence of bidirectional phase curves of size-sorted geologic samples was recently analyzed by *Schröder et al.* [2011] and the spectral behavior of the retrieved Hapke parameters was described in detail by *Johnson et al.* [2013]. Our own observations, in particular the shape of the spectral ratio curves seen on Figure 6, are entirely consistent with these results and, as such, will not be the subject of a detailed discussion here. *Johnson et al.* [2013] summarize and discuss some explanations proposed in the literature for the spectral dependence of bidirectional properties. Most of explanations for phase reddening can be formulated in terms of spectral evolutions of the optical path length and resulting evolution of the volume / surface scattering ratio (i.e., the relative contribution of multiple reflections versus surface scattering) with phase angle. The reddening observed when phase angle increases from 0° to about 70–80° is attributed to the increasing contribution of multiple scattering

with increasing phase angle. The "arch" shape of the ratio curves caused by the falloff of the ratio values beyond 80° of phase angle ("phase bluing") could be due to the opposite effect, i.e., a relative increase of surface scattering versus volume scattering when phase angle increases beyond 80°. *Schroder et al.* [2011] show that geometric optics simulations can indeed correctly reproduce this arch shape, at least for some of the samples investigated.

4.3. On the Characterization of Wet and Icy Soils by Visible Photometry

[78] Results of our measurements of wet and icy soils analogs reveal that their distinct photometric properties can be used as signatures to identify and characterize such soils on Mars. The general darkening of the sample as liquid water is added is a well-known effect, previously quantitatively described by *Gunderson et al.* [2007]. New measurements reported in this study provide additional details about this photometric effect. Wetting and drying experiments show in particular that, at low phase angle, the decrease of reflectance caused by liquid water is not strongly dependent on the amount of water until a thick film of water forms and a specular peak appears. The situation is different at high phase angle as the intensity of the forward-scattering peak shows a strong dependence on the amount of water. In addition to being relatively independent of water content, the ratio between the reflectance of the wet and dry samples at low phase angle seems relatively constant from one sample to another, in the range of 0.35 to 0.45 at a wavelength of 650 nm. As a consequence, a simple quantification of the ratio of reflectance
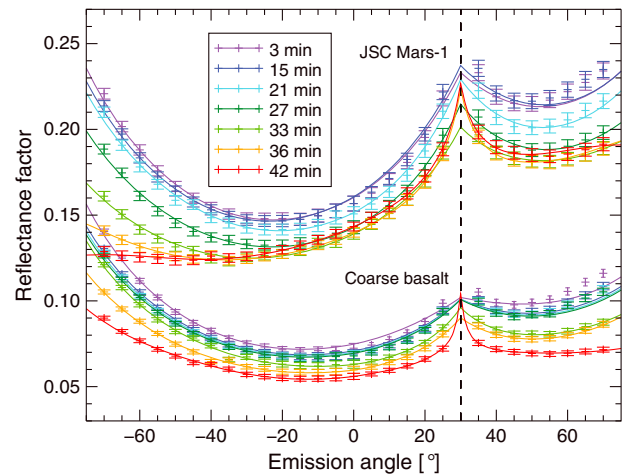
Figure 17. Temporal evolution of the bidirectional reflectance factor of a JSC Mars-1 sample (top group of curves) and a coarse basalt sample (bottom group of curves) covered by decreasing amounts of fine H_2O frost. All measurements (symbols) were acquired at the wavelength: $\lambda = 650$ nm in the principal plane. The solid curves are calculated from the Hapke coefficients (provided in Table 8) obtained by fitting the Hapke photometric model to the measured data. The frost was directly condensed at the surface of the grains (Figure 16) from atmospheric water vapor at ambient temperature (293 K) and is slowly subliming in the dry environment of the freezer, resulting in a rapid decrease of the reflectance factor in the forward-scattering direction.

Table 8. Hapke Parameters Calculated for Seven Steps of the Defrosting Sequences of the JSC Mars-1 and Coarse Basalt Surfaces. These Coefficients Correspond to the Principal Plane Curves Shown in Figure 17[a]

|	ω	h_s	B_s	$\overline{\theta}$ (°)	b	c	χ^2_{red}
			JSC Mars-1				
Step 1	0.391	0.506	5.0	0	0.248	−0.832	**1.1**
	(0.35, 0.45)	(0.35, 0.84)	(>3.8)	(<10)	(0.18, 0.30)	(−0.95, −0.75)	
Step 2	0.386	0.477	5.0	0	0.235	−0.815	**1.2**
	(0.35, 0.44)	(0.34, 0.77)	(>3.8)	(<10)	(0.16, 0.29)	(−0.93, −0.76)	
Step 3	0.396	0.382	5.0	0	0.205	−0.913	**0.5**
	(0.36, 0.50)	(0.37, 0.56)	(>4.9)	(<11)	(0.14, 0.22)	(−0.92, −0.78)	
Step 4	0.458	0.324	2.9	3.7	0.202	−0.748	**0.3**
	(0.33, 0.57)	(0.31, 0.54)	(-)	(<12)	(0.11, 0.25)	(<−0.48)	
Step 5	0.496	0.248	1.18	0	0.198	−0.247	**0.4**
	(0.49, 0.56)	(<0.49)	(-)	(<7)	(0.08, 0.34)	(<0.1)	
Step 6	0.505	0.061	0.74	6.5	0.182	0.479	**0.1**
	(0.41, 0.54)	(<0.35)	(0.46, 1.86)	(<15)	(0.02, 0.27)	(>0.03)	
Step 7	0.496	0.056	0.659	13.0	0.166	0.871	**0.1**
	(0.39, 0.54)	(<0.44)	(0.36, 1.91)	(<19)	(0.03, 0.26)	(>0.21)	
			Coarse Basalt				
Step 1	0.256	0.741	5.0	0	0.379	−0.940	**2.7**
	(0.22, 0.31)	(>0.42)	(>3.9)	(<9)	(0.33, 0.41)	(−0.99, −0.90)	
Step 2	0.268	0.469	5.0	0	0.344	−0.975	**1.7**
	(0.23, 0.31)	(0.34, 0.91)	(>3.7)	(<9)	(0.29, 0.39)	(<−0.92)	
Step 3	0.268	0.431	5.0	0	0.334	−0.982	**1.5**
	(0.23, 0.31)	(0.31, 0.79)	(>3.6)	(<9)	(0.29, 0.39)	(<−0.93)	
Step 4	0.266	0.421	5.0	0	0.329	−0.983	**1.5**
	(0.23, 0.31)	(0.31, 0.76)	(>3.6)	(<9)	(0.28, 0.38)	(<−0.93)	
Step 5	0.404	0.178	2.32	0	0.358	−0.977	**0.5**
	(0.32, 0.47)	(<0.37)	(>1.1)	(<15)	(0.26, 0.66)	(<−0.87)	
Step 6	0.297	0.271	3.0	1.3	0.263	−1.0	**0.3**
	(0.22, 0.41)	(<0.48)	(-)	(<13)	(0.19, 0.32)	(<−0.77)	
Step 7	0.455	0.016	1.17	21	0.438	−0.876	**0.2**
	(0.27, 0.51)	(<0.70)	(-)	(18, 28)	(0.30, 0.59)	(<−0.79)	

[a]Contrary to all other samples, the parameter B_s was allowed to reach values larger than 1 and up to 5 for these two samples, as constraining this parameter values to a maximum of 1 prevented any good fitting of the data.

between a dry soil and a putative wet soil on Mars could already provide a strong indication for the presence or absence of liquid water in the soil. The situation might be complicated, however, by subpixel mixtures between dry and wet areas and by local variations of composition and texture that will strongly affect the measured ratio.

[79] A major difficulty in this study is the quantification of liquid water in the top layer of the soil simulants. Because of the diffusion of water through the sample and the constant drying at the surface exposed to the atmosphere, mass measurements only provide values of the bulk average amount of water and this is likely to be different from the one at the very surface that influences the light reflection. As a consequence, the amount of water can only be described here in qualitative terms by describing the aspect of the surface observed under the optical microscope. It could be useful in the future to redo these experiments while accurately quantifying the amount of water in the surface layer of the sample. Near-infrared or dielectric spectroscopies would be appropriate tools for such measurements.

[80] In addition to the overall decrease of reflectance, the strong reduction of the backscattering peak intensity and the strong increase of the forward-scattering peak intensities are clear photometric signatures of liquid water. As a consequence, the acquisition of high-resolution images in two or three carefully chosen geometries, one close to zero phase angle, one at moderate (30–60°) and one at high (>100°) phase angle, would definitely help in firmly identifying liquid water and ice in the Martian soils. On the other hand, the

search for specular reflections is certainly not the best strategy to look for liquid water as a specular peak is only observed when a large amount of water is present at the surface of the sample, a situation that is unlikely on present-day Mars given the current atmospheric conditions. Regarding the contamination of surface photometric signatures by atmospheric aerosols,
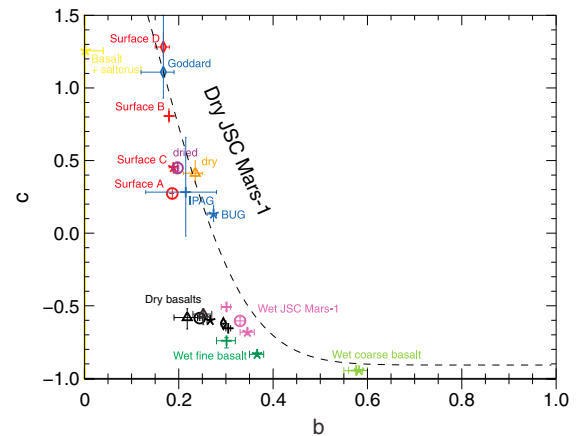
Figure 18. Relation between the b and c parameters obtained by fitting the Hapke model to measured data for dry and wet samples. The dashed line represents the empirical "hockey stick" relation as proposed by *Hapke* [2012]. Note that this relation, as defined by Hapke, also has a certain width across the central line, not shown here for clarity.
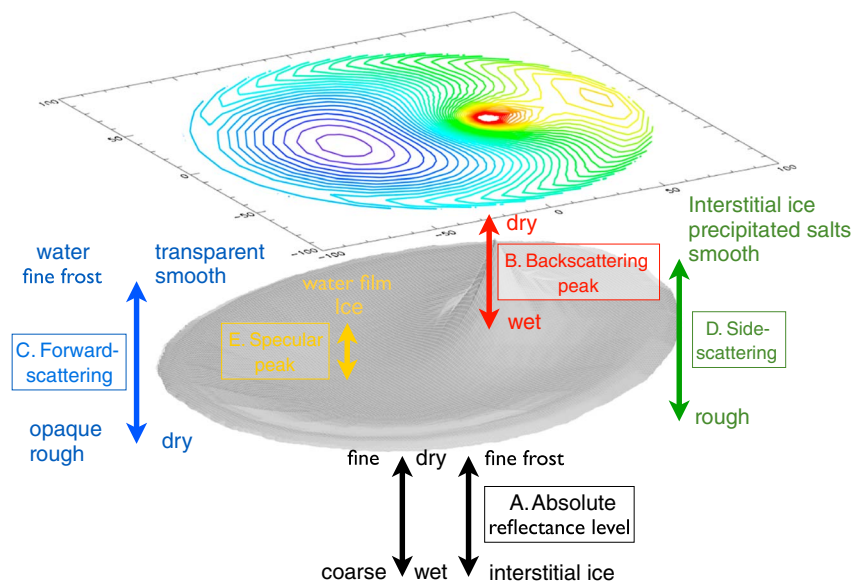
Figure 19. Schematic summary of most of the photometric effects reported and discussed in this paper. The 3D surface and the color contour lines on top represent a "standard" bidirectional reflectance plot at a fixed incidence angle: i = 30° and a fixed wavelength: λ = 650 nm, in this case a dry surface prepared from JSC Mars-1 (calculated using the Hapke coefficients provided in Table 1). The various arrows show which regions of the bidirectional phase function are affected by different parameters.

photometric criteria based on measurements at low to moderate phase angles are more suitable as atmospheric aerosols show a strong forward scattering. As a result, the disappearance of the ubiquitous backscattering peak in wet soils is a less ambiguous visible photometric criterion to look for liquid water in the upper Martian soil from orbit.

[81] An interesting potential implication of these results is the case of the "RSL" (Recurring Slope Lineae) features [*McEwen et al.*, 2011; *Chevrier and Rivera-Valentin*, 2012; *Levy*, 2012]. The RSLs observed in 2007 were the ones showing the highest contrast with the surroundings soils, being darker by about 40% (in units of I/F after an atmospheric correction) in the broad RED band pass (550–850 nm), as well as in the BG (400–600 nm) and IR (800–1000 nm) color bands. This is the result of the planet-encircling dust storm that had deposited a thin coating of bright dust on all terrains. This bright coating was later affected by RSL activity, causing high photometric contrast. The contrast of reflectance between RSL and surrounding soils is generally lower in subsequent years, but poorly quantified as the atmospheric correction of HiRISE images has not yet been performed.

[82] According to our photometric measurements of wet soils, this darkening appears too low to be interpreted by the effect of liquid water, as even minute amount of liquid water should lower the reflectance by more than a factor of two in the wide RED band pass of HiRISE. It is, however possible, as already briefly mentioned, that the RSLs areas are not homogeneous. A subpixel geographic mixture with 70% of the RSL area being wet and 60% darker than the surrounding soil could account for the observed decrease of reflectance of 40% on HiRISE images. However, no infrared spectral signature of water was identified by the CRISM near-infrared spectrometer. Reasons for the absence of detection of water might be the spatial resolution of the instrument

that is insufficient to resolve the dark features and/or the weakness of H_2O absorptions due to the expected small quantities of water by midafternoon when the CRISM data were acquired [*Massé et al.*, 2012]. This work suggests a variety of tests or consistency checks for a soil wetting origin of RSL based on color and photometric behaviors, when quantitative photometric analyses of HiRISE data, atmospheric correction and refined radiometric calibration, have been completed. Observations at low phase angles are also clearly useful to distinguish wet and dry surfaces—the RSL contrast should be greatest at low phase angles if the darkening is due to wetting. Observation in the early morning is by far the best time to detect brines on Mars, given the deliquescence and efflorescence observed in laboratory experiments [*Gough et al.*, 2011] but that is not currently possible with Mars Reconnaissance Orbiter.

[83] After drying out, the samples usually display photometric properties that are different from their initial dry state. Two possible reasons for this are (1) the modification of the surface texture as a result of alignment and flattening of the grains and (2) the crystallization of previously dissolved salts. It is difficult to distinguish between these two processes by their bidirectional reflectance signature, as they appear relatively similar. As a consequence, the observation of a brighter surface after drying cannot be uniquely interpreted in terms of the crystallization of salts but could also be attributed to a change in the microtexture of the surface.

[84] In a similar way, icy soils could be recognized by their bidirectional photometric signature, which is clearly distinct from the ones of both dry and wet soils. The presence of a fine water frost condensed from atmospheric water vapor at the surface of the grains will inhibit the specular reflection and cause strong forward scattering. Because the photometric properties of icy soils are so strongly dependent on the
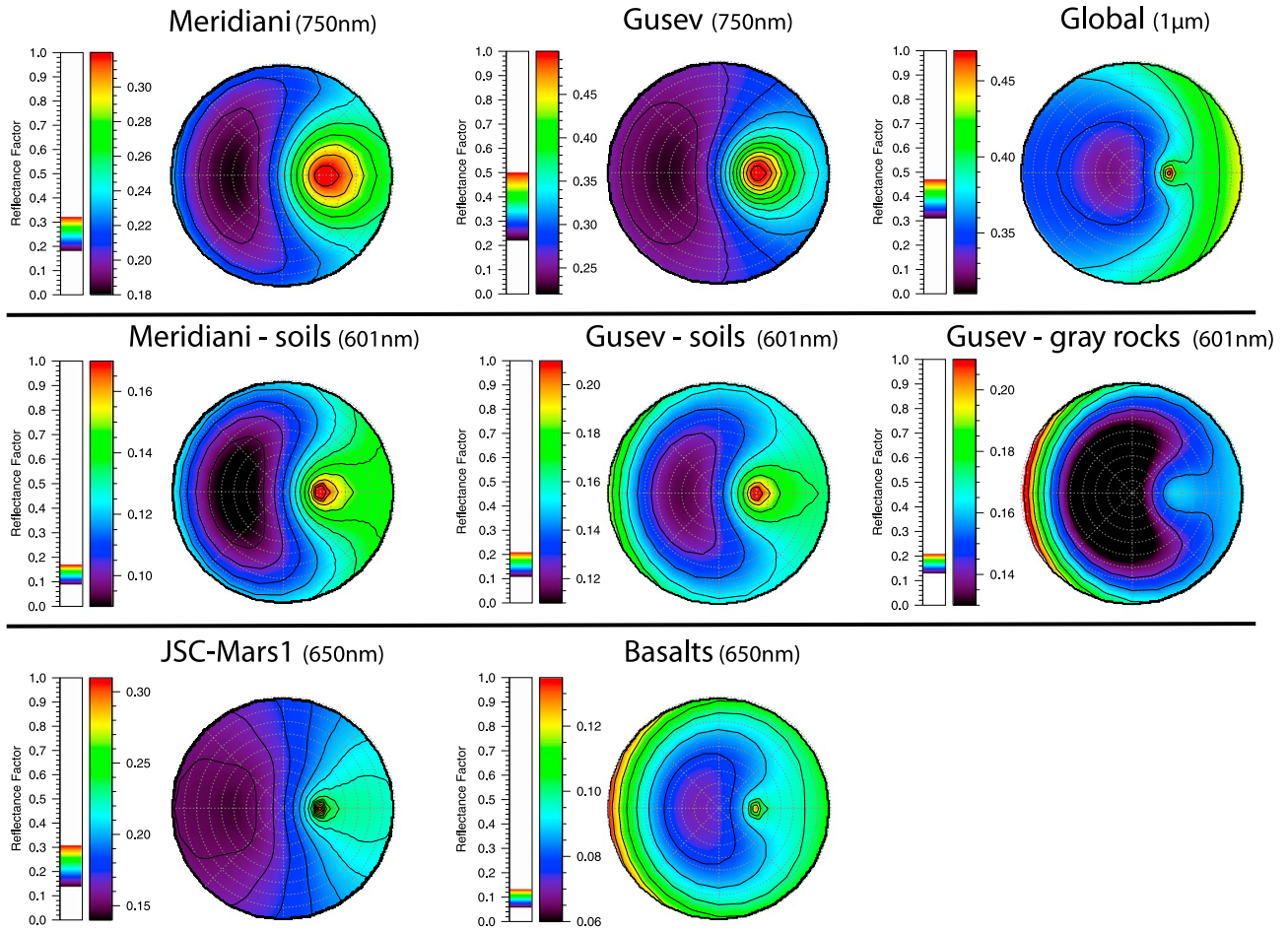
Figure 20. Comparison between the photometric behaviors of the JSC Mars-1 and basaltic sand analogs (bottom), the Martian surface at MERs landing sites, as determined from in situ PANCAM observations (middle) and CRISM orbital observations (top) and an average global photometric behavior ("global", top). All reflectance factors values were calculated from sets of Hapke parameters published by *Johnson et al.* [2006a] for Gusev grey rocks and Gusev soils, *Johnson et al.* [2006b] for Meridiani soils, *Fernando et al.* [2013] for Gusev and Meridiani regions from CRISM, and *Vincendon* [2013] for the average global behavior. Most of reflectance values shown here were averaged from data sets acquired for similar samples or surfaces (all JSC Mars-1 surfaces for which Hapke coefficients are reported in Tables 1 and 2; All basalt surfaces for which Hapke coefficients are reported in Table 3; all soils and grey rocks in Gusev and all soils in Meridiani for PANCAM data; all regions of interest in Gusev for CRISM data). The reflectance values are displayed in a similar way as for the laboratory measurements presented in previous figures, for a fixed incidence angle: $i = 30°$. Note the different wavelengths at which measurements were obtained that could result in differences between the data sets, especially in terms of the absolute values of the reflectance factors.

physical state of the ice, multiangular observations have potential for refining the mapping of surface ice on Mars. The contrast of reflectance between interstitial ground ice and surface frost deposited from atmospheric water vapor has already been used to distinguish these two types of ices in images obtained by the Phoenix lander at high Northern latitude on Mars [*Smith et al.*, 2009]. However, because of the multitude of possible associations between soils and water ice, more experiments should be conducted in the future to investigate alternative textures of icy soils. In particular, future studies should address the case of Martian snowfalls, as *Vincendon et al.* [2010] suggest that precipitation of atmospheric water ice contributes greater to surface frost than direct condensation of water vapor at the surface.

4.4. Spectral and Bidirectional Effects

[85] As illustrated here and in multiple previous articles, retrieving information on the physical and chemical properties of the surface from multiangular observations and visible / near-infrared reflectance spectroscopy is challenging as different properties of the sample can affect its optical properties in indistinguishable ways. However, information retrieved by comparing the reflectance in different geometries and at different wavelengths can be ideally combined to better constrain the state of the surface. For example, we have shown here that the near-infrared spectral signature of H_2O at 1 µm appears stronger in the fraction of light scattered in the forward and specular directions whereas the red color of the sample is attenuated in these same directions.

[86] Combining color and multidirectional observations of the surface of Mars could as well provide more confidence in identifying liquid water from its photometric properties. Color stereo imaging is regularly used to obtain digital elevation models of the surface at meters to decameters spatial scales and new instruments are currently being designed for missions to Mars and other Solar System targets. In addition to the pair of images required for digital terrain model extraction, the acquisition of a color image at a phase angle close to 0 would be extremely valuable to assess various properties of the surface and in particular to obtain robust indications of the presence of small amounts of liquid water in the regolith. High-resolution (5 m/pixel) color observations that vary with time of day during season, as expected from the ESA Trace Gas Orbiter CASSIS instrument, could be particularly valuable.

5. Conclusion

[87] We have measured in the laboratory the visible bidirectional reflectance factors of Mars surface analogs under a large variety of geometries. Measurements of volatile-free samples allowed us to investigate the influence of surface texture on the photometric properties. This influence is significant for samples with opaque particles but is considerably reduced in the case of samples with transparent particles. The comparison of four independent measurements of samples of JSC Mars-1 soil simulant conducted by four different teams with five different instruments shows differences that can be attributed to differences in the surface texture of the samples, resulting from different preparation procedures. Despite these minor discrepancies, the reproducibility of bidirectional reflectance measurements is satisfactory.

[88] The comparison between the photometric behaviors of the JSC Mars-1 sample and the Hawaiian basaltic sand shows interesting similarities with photometric observations at the surface of Mars. The pronounced broad backscattering peak, present for all our dry samples, has been observed in situ for all Martian materials by the Pathfinder Lander and Mars Exploration Rovers. In addition, these observations show a contrast of behaviors at high phase angle with the presence of a limited forward-scattering peak in the case of less dusty rocks and compacted soils. Our experiments reproduce this photometric contrast, as forward-scattering peak is observed for both the fine and coarse particle size fractions of basalt and for the smoothest surfaces made of the JSC Mars-1 soil simulant.

[89] Photometric measurements of wet samples show the strong influence of the presence of liquid water on the photometric properties of soils, both in terms of absolute level of reflectance and shape of the reflectance distribution function. Introduction of liquid water, even in relatively low amount, results in the disappearance of the backscattering peak and the appearance of a forward-scattering peak whose intensity increases with the amount of water introduced. Specular reflections only appear when water is present in an amount large enough to allow water to form a film at the surface of the sample. When there is enough water to form a thick and flat film, the specular peak is very narrow. When the amount of water is lower, the liquid film conforms to the topography of the underlying grains, which results in a very broad specular peak, which coexists and can partially merge with the forward-scattering peak. Because of the strong contrast of

photometric behavior between all dry materials at Mars surface and putative wet soils, imaging of dark soils under two or three different geometric conditions could provide supporting evidence for liquid water in the Martian regolith by its photometric signature. The set of measurements would ideally include one image at a phase angle as low as possible (10° or less), one at a moderate phase angle (20–60°) and, if possible, one at high phase angle (>90°).

[90] The presence of water ice at the soil surface can variably affect the photometry of the soil, depending on the form of association between water and minerals. Mapping of photometric criteria of the surface in Mars polar regions could thus be used to decipher the presence and state of water in the ground. More extensive laboratory work involving additional procedures to prepare various types of icy soils in a reproducible way will first be necessary to establish firm relationships between photometric parameters and the properties of the icy soils.

[91] Multiangular observations have significant potential to better constrain the composition and physical state of material at the surface of Mars. Orbital remote-sensing determination of the surface photometric properties has for long been prevented by difficulties to distinguish contributions from the surface and the atmosphere. Recent progress on the correction of atmospheric effects using CRISM multiangular observations now pave the way to an accurate retrieval of the surface bidirectional reflectance properties. Laboratory measurements of the photometry of close analogs for Mars surface materials will be crucial to test the accuracy of their inversion procedure. Systematic and nearly simultaneous measurements of a selected target under multiple geometries would be a significant addition to the capabilities of future high-resolution imaging systems for Mars.

References

Allen, C. C., R. V. Morris, D. J. Lindstrom, M. M. Lindstrom, and J. P. Lockwood (1997), JSC Mars-1 - Martian regolith simulant. *Lunar and Planetary Science Conference*, 28, Abstract 1797.
Bandfield, J. L. (2002), Global mineral distributions on Mars, *J. Geophys. Res.*, *107*(E6), 5042, doi:10.1029/2001JE001510.
Beck, P., A. Pommerol, N. Thomas, B. Schmitt, F. Moynier, and J. -A. Barrat (2012), Photometry of meteorites, *Icarus*, *218*, 364–377.
Brissaud, O., B. Schmitt, N. Bonnefoy, S. Douté, P. Rabou, W. Grundy, and M. Fily (2004), Spectrogonio Radiometer for the study of the bidirectional reflectance and polarizations functions of planetary surfaces. 1. Design and tests, *Appl. Opt.*, *43*, 1926–1937.
Byrne, S., et al. (2009), Distribution of Mid-Latitude Ground Ice on Mars from New Impact Craters, *Science*, *325*, 1674–1676.
Ceamanos, X., S. Douté, J. Fernando, F. Schmidt, P. Pinet, and A. Lyapustin (2013), Surface reflectance of Mars observed by CRISM/MRO: 1. Multi-angle approach for retrieval of surface reflectance from CRISM observations (MARS-ReCO), *J. Geophys. Res. Planets*, *118*, 514–533, doi:10.1029/2012JE004195.
Chevrier, V., and E. G. Rivera-Valentin (2012), Formation of recurring slope lineae by liquid brines on present-day Mars, *Geophys. Res. Lett.*, *39*, L21202, doi:10.1029/2012GL054119.
Clancy, R. T., and S. W. Lee (1991), A new look at dust and clouds in the Mars atmosphere - Analysis of emission-phase-function sequences from global Viking IRTM observations, *Icarus*, *93*, 135–158.
Clancy, R. T., M. J. Wolff, and P. R. Christensen (2003), Mars aerosol studies with the MGS TES emission phase function observations: Optical depths, particle sizes, and ice cloud types versus latitude and solar longitude, *J. Geophys. Res.*, *108*(E9), 5098, doi:10.1029/2003JE002058.

Cord, A. M., P. C. Pinet, Y. Daydou, and S. D. Chevrel (2003), Planetary regolith surface analogs: optimized determination of Hapke parameters using multi-angular spectro-imaging laboratory data, *Icarus*, *165*, 414–427.

Cord, A., P. Pinet, Y. Daydou, and S. Chevrel (2005), Experimental determination of the surface photometric contribution in the spectral reflectance deconvolution processes for a simulated martian crater-like regolithic target, *Icarus*, *175*, 78–91.

Cull, S. C., R. E. Arvidson, J. G. Catalano, D. W. Ming, R. V. Morris, M. T. Mellon, and M. Lemmon (2010), Concentrated perchlorate at the Mars Phoenix landing site: Evidence for thin film liquid water on Mars, *Geophys. Res. Lett.*, *37*, L22203, doi:10.1029/2010GL045269.

Feldman, W. C., et al. (2004), Global distribution of near-surface hydrogen on Mars, *J. Geophys. Res.*, *109*, E09006, doi:10.1029/2003JE002160.

Fernando, J., F. Schmidt, X. Ceamanos, P. Pinet, S. Douté, and Y. Daydou (2013), Surface reflectance of Mars observed by CRISM/MRO : 2. Estimation of surface photometric properties in Gusev Crater and Meridiani Planum, *J. Geophys. Res. Planets*, *118*, 534–559, doi:10.1029/201JE004194.

Geissler, P. E. (2005), Three decades of Martian surface changes, *J. Geophys. Res.*, *110*, E02001, doi:10.1029/2004JE002345.

Georgiev, G. T., and J. J. Butler (2005), Bidirectional reflectance distribution function and directional-hemispherical reflectance of a martian regolith simulant, *Opt. Eng.*, *44*(**3**), 036202, doi:10.1117/1.1870001.

Gough, R. V., V. F. Chevrier, K. J. Baustian, M. E. Wise, and M. A. Tolbert (2011), Laboratory studies of perchlorate phase transitions: Support for metastable aqueous perchlorate solutions on mars, *Earth Planet. Sci. Lett.*, *312*, 371–377.

Gunderson, K., N. Thomas, and J. A. Whitby (2006), First measurements with the Physikalisches Institut Radiometric Experiment (PHIRE), *Planet. Space Sci.*, *54*, 1046–1056.

Gunderson, K., B. Lüthi, P. Russel, and N. Thomas (2007), Visible/NIR photometric signatures of liquid water in Martian regolith simulant, *Planet. Space Sci.*, *55*, 1272–1282.

Hamilton, V. E., R. V. Morris, J. E. Gruener, and S. A. Mertzman (2008), Visible, near-infrared, and middle infrared spectroscopy of altered basaltic tephras: Spectral signatures of phyllosilicates, sulfates, and other aqueous alteration products with application to the mineralogy of the Columbia Hills of Gusev Crater, Mars, *J. Geophys. Res.*, *113*, E12S43, doi:10.1029/2007JE003049.

Hapke, B. (1993), Theory of Reflectance and Emittance Spectroscopy, Topics in Remote Sensing, Cambridge, U. K.

Hapke, B. (2002), Bidirectional reflectance spectroscopy 5, *The coherent backscatter opposition effect and anisotropic scattering, Icarus*, *157*, 523–534.

Hapke, B. (2012), Bidirectional reflectance spectroscopy 7. The single particle phase function hockey stick relation, *Icarus*, *221*, 1079–1083.

Hapke, B. (2013), Comment on "A critical assessment of the Hapke photometric model" by Y. Shkuratov et al, *J. Quant. Spectrosc. Radiat. Transfer*, *116*, 184–190.

Hapke, B., M. K. Shepard, R. Nelson, W. Smythe, and J. Piatek (2009), A quantitative test of the ability of models based on the equation of radiative transfer to predict the bidirectional reflectance of a well-characterized medium, *Icarus*, *199*, 210–218.

Hapke, B., B. Denevi, H. Sato, S. Braden, and M. Robinson (2012), The wavelength dependence of the lunar phase curve as seen by the Lunar Reconnaissance Orbiter wide-angle camera, *J. Geophys. Res.*, *117*, E00H15, doi:10.1029/2011JE003916.

Helfenstein, P., and M. K. Shepard (2011), Testing the Hapke photometric model: Improved inversion and the porosity correction, *Icarus*, *215*, 83–100.

Henyey, L. C., and J. L. Greenstein (1941), Diffuse radiation in the galaxy, *Astrophys. J.*, *93*, 70–83.

Johnson, J. R., et al. (1999), Preliminary results on photometric properties of materials at the Sagan Memorial Station, Mars, *J. Geophys. Res.*, *104*, 8809–8830.

Johnson, J. R., et al. (2006a), Spectrophotometric properties of materials observed by Pancam on the Mars Exploration Rovers: 1. Spirit, *J. Geophys. Res.*, *111*, E02S14, doi:10.1029/2005JE002494.

Johnson, J. R., et al. (2006b), Spectrophotometric properties of materials observed by Pancam on the Mars Exploration Rovers: 2. Opportunity, *J. Geophys. Res.*, *111*, E12S16, doi:10.1029/2006JE002762.

Johnson, J. R., J. F. Bell, P. Geissler, W. M. Grundy, E. A. Guinness, P. C. Pinet, and J. Soderblom (2008), Physical properties of the Martian surface from spectrophotometric observations, in *The Martian Surface – Composition, Mineralogy and Phyiscal Properties*, edited by J. Bell III, pp. 428, Cambridge University Press, Cambridge, United Kingdom.

Johnson, J. R., M. K. Shepard, W. M. Grundy, D. A. Paige, and E. Foote (2013), Spectrogoniometry and modeling of martian and lunar analog samples and Apollo soils, *Icarus*, *223*, 383–406.

Jost, B., B. Gundlach, A. Pommerol, J. Oesert, S. N. Gorb, J. Blum, and N. Thomas (2013), Micrometer-sized ice particles for planetary-science experiments - II. Bidirectional reflectance, *Icarus*, *225*, 352–366.

Kaasalainen, S. (2003), Laboratory photometry of planetary regolith analogs. I. Effects of grain and packing properties on opposition effect, *A & A*, *409*, 765–769.

Kennedy, J., and R. C. Eberhard (2001), *Swarm Intelligence*, 512 pp., Morgan Kaufmann Publishers, San Francisco, CA, USA.

Kirk, R. L., et al. (1999), Digital photogrammetric analysis of the IMP camera images: Mapping the Mars Pathfinder landing site in three dimensions, *J. Geophys. Res.*, *104*, 8869–8888, doi:10.1029/1998JE900012.

Lekner, J., and M. C. Dorf (1988), Why some things are darker when wet, *Appl. Opt.*, *27*, 1278–1280.

Levy, J. S. (2012), Hydrological characteristics of recurrent slope linae on Mars: Evidence for liquid flow through regolith and comparisons with Antarctic terrestrial analogs, *Icarus*, *219*, 1–4.

Levy, J. S., A. G. Fountain, K. A. Welch, and W. M. Lyons (2012), Hypersaline "wet patches" in Taylor Valley, Antarctica, *Geophys. Res. Lett.*, *39*, L05402, doi:10.1029/2012GL050898.

Markwardt, C. B. (2009), Non-linear least squares fitting in IDL with MPFIT, in *proc. Astronomical Data Analysis Software and Systems*, 18, 251-254.

Marquardt, D. (1963), An algorithm for least-squares estimation of nonlinear parameters, *SIAM J. Appl. Math.*, *11*, 431–441.

Massé, M., P. Beck, B. Schmitt, A. Pommerol, A. McEwen, V. F. Chevrier, and O. Brissaud (2012), Nature and origin of RSL: Spectroscopy and detectability of liquid brines on the near-infrared, *Lunar and Planetary Science Conference*, 43, Abstract 1856.

McEwen, A. S., O. Lujendra, C. M. Dundas, S. S. Mattson, S. Byrne, J. J. Wray, S. C. Cull, S. L. Murchie, N. Thomas, and V. C. Gulick (2011), Seasonal flows on warm Martian slopes, *Science*, *333*, 740–743.

McGuire, A. F., and B. W. Hapke (1995), An experimental study of light scattering by large, irregular particles, *Icarus*, *113*, 134–155.

Mishchenko, M. I., L. D. Travis, and D. W. Mackowski (1996), T-matrix computations of light scattering by nonspherical particles: A review, *J. Quant. Spectrosc. Radiat. Transfer*, *55*, 535–575.

Moré, J. (1978), The Levenberg-Marquardt algorithm: implementation and theory, *Numerical Analysis*, *630*, 105.

Morris, R. V., T. D. Shelfer, A. C. Scheinost, N. W. Hinman, G. Furniss, S. A. Mertzman, J. L. Bishop, D. W. Ming, C. C. Allen, and D. T. Britt (2000), Mineralogy, composition, and alteration of Mars Pathfinder rocks and soils: Evidence from multispectral, elemental, and magnetic data on terrestrial analogue, SNC meteorite, and Pathfinder samples, *J. Geophys. Res.*, *105*, 1757–1818.

Nelson, R. M., W. D. Smithe, B. W. Hapke, and A. S. Hale (2002), Low phase angle laboratory studies of the opposition effect: search for wavelength dependence, *Planet. Space Sci.*, *50*, 849–856.

Piatek, J. L., B. W. Hapke, R. M. Nelson, W. D. Smythe, and A. S. Hale (2004), Scattering properties of planetary regolith analogs, *Icarus*, *171*, 531–545, doi:10.1016/j.icarus.2004.05.019.

Pommerol, A., and B. Schmitt (2008), Strength of the H_2O near-infrared absorption bands in hydrated minerals: effects of measurement geometry, *J. Geophys. Res.*, *113*, E12008, doi:10.1029/2008JE003197.

Pommerol, A., G. Portyankina, N. Thomas, K. -M. Aye, C. J. Hansen, M. Vincendon, and Y. Langevin (2011a), Evolution of south seasonal cap during Martian spring: Insights from high-resolution observations by HiRISE and CRISM on Mars Reconnaissance Orbiter, *J. Geophys. Res.*, *116*, E08007, doi:10.1029/2010JE003790.

Pommerol, A., N. Thomas, M. Affolter, G. Portyankina, B. Jost, and K. –. M. Aye (2011b), Photometry and bulk physical properties of Solar System surfaces icy analogs: The Planetary Ice Laboratory at University of Bern, *Planet. Space Sci.*, *59*, 1601–1612.

Pommerol, A., T. Appéré, G. Portyankina, K. –. M. Aye, N. Thomas, and C. J. Hansen (2013), Observations of the northern seasonal polar cap on Mars III: CRISM/HIRISE observations of spring sublimation, *Icarus*, *225*(2), 911–922.

Poulet, F., C. Gomez, J. –. P. Bibring, Y. Langevin, B. Gondet, P. Pinet, G. Belluci, and J. Mustard (2007), Martian surface mineralogy from Observatoire pour la Minéralogie, l'Eau, les Glaces et l'Activité on board the Mars Express spacecraft (OMEGA/MEx): Global mineral maps, *J. Geophys. Res.*, *112*, E08S02, doi:10.1029/2006JE002840.

Schroder, S. E., Y. Grynko, A. Pommerol, and H. U. Keller (2011), Phase reddening observed in the laboratory, *EPSC-DPS Joint Meeting*, 6, Abstract 1841.

Shepard, M. K., and P. Helfenstein (2007), A test of the Hapke photometric model, *J. Geophys. Res.*, *112*, E03001, doi:10.1029/2005JE002625.

Shkuratov, Y., L. Starukhina, H. Hoffmann, and G. Arnold (1999), A model of spectral albedo of particulate surfaces: Implications for optical properties of the Moon, *Icarus*, *137*, 235–246.

Shkuratov, Y., A. Ovcharenko, E. Zubko, O. Miloslavskaya, K. Muinonen, J. Piironen, R. Nelson, W. Smythe, V. Rosenbush, and P. Helfenstein

(2002), The Opposition Effect and Negative Polarization of Structural Analogs for Planetary Regoliths, *Icarus*, *159*, 396–416, doi:10.1006/icar.2002.6923.

Shkuratov, Y., V. Kaydash, V. Korokhin, Y. Velikodsky, D. Petrov, E. Zubko, D. Stankevich, and G. Videen (2012), A critical assessment of the Hapke photometric model, *J. Quant. Spectrosc. Radiat. Transfer*, *113*, 2431–2456.

Smith, P. H., et al. (2009), H_2O at the Phoenix landing site, *Science*, *325*, 58–61.

Souchon, A. L., P. C. Pinet, S. D. Chevrel, D. H. Daydou, D. Baratoux, K. Kurita, M. K. Shepard, and P. Helfenstein (2011), An experimental study of Hapke's modeling of natural granular surface samples, *Icarus*, *215*, 313–331.

Stillman, D. E., and R. E. Grimm (2011), Dielectric signatures of adsorbed and salty liquid water at the Phoenix landing site, Mars, *J. Geophys. Res.*, *116*, E09005, doi:10.1029/2011JE003838.

Twomey, S. A., C. F. Bohren, and J. L. Mergenthaler (1986), Reflectance and albedo differences between wet and dry surfaces, *Appl. Opt.*, *25*, 431–437.

Vincendon, M., F. Forget, and J. Mustard (2010), Water ice at low to midlatitudes on Mars, *J. Geophys. Res.*, *115*, E10001, doi:10.1029/2010JE003584.

Vincendon, M. (2013), Mars surface phase function constrained by orbital observations, *Planet. Space Sci.*, *76*, 387–95.

Vincendon, M., Y. Langevin, F. Poulet, A. Pommerol, M. Wolff, J. P. Bibring, B. Gondet, and D. Jouglet (2009), Yearly and seasonal variations of low albedo surfaces on Mars in the OMEGA/MEx dataset: Constraints on aerosols properties and dust deposits, *Icarus*, *200*, 395–405.

Zhang, H., and K. J. Voss (2006), Bidirectional reflectance study on dry, wet, and submerged particulate layers: effects of pore liquid refractive index and translucent particle concentrations, *Appl. Opt.*, *34*, 8753–8763.